*Journal of Wind Engineering and Industrial Aerodynamics*, 21 (1985) 119—154
Elsevier Science Publishers B.V., Amsterdam — Printed in The Netherlands



# NUMERICAL STUDIES OF FLOW THROUGH A WINDBREAK

JOHN D. WILSON*

*University of Guelph, Guelph, Ontario N1G 2W1 (Canada)*

(Received August 27, 1984)

## Summary

The pattern of flow through a porous windbreak has been investigated numerically using several well-known closure schemes (turbulence models). The shelter is included as a momentum extraction term in the streamwise momentum equation, for a fence having the value $k_r\bar{u}|\bar{u}|\delta(x,0)\,s(z,H)$ where $k_r$ is the pressure-loss coefficient of the fence, $\bar{u}$ is the local mean horizontal ($x$) velocity, $\delta(x,0)$ is the delta function and $s(z,H)$ is a unit step function which is zero for heights ($z$) greater than the fence height, $H$. Previous experiments on neutrally stratified surface-layer flow through a porous fence were numerically simulated. Very good agreement with the observed velocity deficit in the near wake ($x \leqslant 15H$ where $H$ = fence height) of the fence was obtained using a Reynolds-stress closure scheme. The predictions of the "$k$—$\epsilon$" closure scheme (which includes turbulent kinetic energy and energy dissipation rate equations to estimate the eddy viscosity) and the simplest scheme tested, eddy viscosity $K = K_0 = ku_{*0}z$ (eddy viscosity at all downwind distances equal to its value far upstream $ku_{*0}z$, where $k$ = von Karman's constant, $u_{*0}$ = friction velocity, $z$ = height) were only slightly less satisfactory. Satisfactory estimates of the pattern of turbulent kinetic energy behind the fence were obtained. All simulations failed to predict the sharp speedup observed over the fence, and consequently yielded a slower rate of recovery towards equilibrium than observed. Attempts to improve prediction of the speed-over and the far wake by including corrections for mean streamline curvature were unsuccessful.

Design aids for isolated windbreaks have been generated from the prediction of the second-order closure model. These give the velocity reduction to be expected in the near wake of the fence and the drag on the fence for a range of values of the fence pressure-loss coefficient, $k_r$.

## I. Introduction

Windbreaks are used all over the world for purposes such as reduction of soil erosion, control of snow drift and provision of a favourable microclimate for humans, animals and plants. There are many types of windbreak in use (stubble strips, trees or shrubs, fences, reed mats, porous cloth) and many factors affect the choice of a windbreak: establishment and maintenance costs, delay in establishment, portability, shading, water use, disease and pest control, to name a few. The value of windbreaks to agriculture and horticulture is incalculably huge, yet present techniques for the design of

*Present address: Meteorology Division, Geography Department, University of Alberta, Edmonton, Alberta T6G 2H4, Canada.

0167-6105/85/$03.30 

windbreaks could hardly be described as quantitative and few would claim that shelter is sufficiently well understood to ensure optimum design.

This paper concentrates solely on the aerodynamic aspects of windbreaks and investigates the problem of calculating the flow pattern which results from placing a porous windbreak perpendicular to the mean stream in an otherwise undisturbed and "ideal" surface-layer flow. Understanding of the effect of a windbreak on the flow pattern (by which is meant both the mean flow and the turbulence) is a prerequisite to a full understanding of other shelter effects (effects on evapotranspiration, leaf and air temperature, relative humidity) as well as being of direct and overriding importance for shelter problems such as soil erosion, snow drift and plant or fruit wind-damage.

The aim of this work is to evaluate turbulence models for the windbreak problem and, where possible, to give design guidelines. In order for the latter to be possible it is essential that the properties of the windbreak itself be specified quantitatively and in a form which can be interpreted from an aerodynamic point of view.

Plate [1] gave a review of shelterbelt aerodynamics. Since that time there have been several contributions, but to the author's knowledge the only attempts to predict shelter flow by solving the fluid flow conservation equations (conservation of mass, momentum and energy) have been those of Hagen et al. [2] (hereafter called HSMK) and Durst and Rastogi [3]. Both these groups solved the equations of motion using a gradient-diffusion closure scheme in which the eddy viscosity was itself modelled (the "$k$—$\epsilon$" model). HSMK, simulating the effect of a porous fence in the atmospheric suface layer, imposed a velocity profile both upstream and in the immediate wake of the fence. Durst and Rastogi, dealing with a solid fence in a wind-tunnel boundary layer, used the no-slip condition at the fence.

It is well known that for barriers of very low porosity the flow pattern is very complex. Often for the purposes of analysis the flow region is partitioned; for example, in their analytical theory for the mean velocity behind an obstacle, Counihan et al. [4] (CHJ) split the wake into a wall zone, a mixing zone, and an external zone. However, for an extremely porous barrier the flow pattern can deviate only very slightly from the well-understood equilibrium surface-layer flow. Practical windbreaks are usually of fairly high porosity (20 to 50% porosity is usually recommended) and may not cause flow separation; in a wind-tunnel study of the flow pattern about solid and porous fences, Perera [5] found that separation occurred only for porosities less than 30%, and that the flow pattern for a given porosity was relatively insensitive to the construction of the model fence*. It therefore seems reasonable to avoid partitioning the flow

---

*That the flow pattern is relatively independent of the fence construction for a given porosity was earlier noted by M. Jensen (Shelter Effect, The Danish Technical Press, Copenhagen, 1954).

and to obtain the entire flow field by solving the equations of motion (with appropriate resolution). The critical question is: are any of the presently available closure schemes ("turbulence models") satisfactory for a windbreak flow?

A detailed examination of the flow through a 50% porous fence carried out by Finnigan and Bradley [6], using as an interpretive framework rigorously derived mean-momentum and turbulent-kinetic-energy (TKE) equations, indicated a rather complex TKE balance in which difficult-to-model terms such as pressure transport (pressure fluctuation—velocity fluctuation correlation) and turbulent transport (velocity triple correlation) played a very important role. This allows little optimism that any present turbulence closure scheme, let alone a first-order (eddy viscosity) closure scheme, could prove very useful for shelter flow. However, HSMK concluded that the first-order $k$—$\epsilon$ model gave satisfactory agreement with their measurements of flow through 20, 40 and 60% porous fences (here it must be remembered that their model was forced to agree with observations at the fence). Similarly, Bradley and Mulhearn [7] concluded that the CHJ analytical solution has some skill at least in predicting the velocity and shear stress profiles far downwind.

Sections II—IV briefly describe the governing equations, a standard numerical method, and a range of well-known closure schemes which were used to predict two-dimensional flows through porous barriers. In Section V the predictions of these models are compared with the experimental data of Bradley and Mulhearn [7]. Section VI gives design guidelines (speed reduction and fence drag as a function of $H/z_0$, $k_r$) based on verified model predictions.

## II. The governing equations and parameterisation of the shelter

Interaction between an airflow and immersed objects (or excluded volumes) necessitates that statistical averaging be carried out with caution. Wilson and Shaw [8] (WS) and Raupach and Shaw [9] (RS) have formally derived the equations of motion for flow through multiply connected space (space within which not every closed contour may be shrunk to a point without crossing solid material). Using RS averaging scheme I we may write the conservation equations for streamwise ($x$) and cross-stream ($z$) momentum and the mass conservation equation in steady-state neutrally stratified incompressible flow as (WS eqn. 3)

$$\frac{\partial}{\partial x}\left(\bar{u}^2 + \overline{u'^2} + \frac{\bar{p}}{\rho}\right) + \frac{\partial}{\partial z}\left(\bar{u}\,\bar{w} + \overline{u'w'}\right) = \mathrm{SU} \tag{1a}$$

$$\frac{\partial}{\partial x}\left(\bar{w}\,\bar{u} + \overline{u'w'}\right) + \frac{\partial}{\partial z}\left(\bar{w}^2 + \overline{w'^2} + \frac{\bar{p}}{\rho}\right) = \mathrm{SW} \tag{1b}$$

$$\frac{\partial \bar{u}}{\partial x} + \frac{\partial \bar{w}}{\partial z} = 0 \tag{1c}$$

Here the overbar denotes a spatial average along the windbreak (cross-wind) over a distance large compared to both the inhomogeneity in the fence/trees and to the largest length-scales of significance in the airflow. The extra terms which arise through this formal averaging procedure and correspond to the form drag and skin friction at the air/solid interfaces have been lumped together in the source terms on the right-hand side since it is necessary that they be parameterised in any case. Viscous diffusion of mean momentum has been neglected, $\bar{p}$ is the departure from a hydrostatic lapse rate and $\rho$ is the density. If the overbar were to be considered to represent the normal Reynolds averaging and SU = SW = 0, one recovers the conventional momentum equations for micrometeorological flow outside any vegetation and away from imbedded obstacles. It is advantageous to derive the governing equations with proper recognition that the flow domain is multiply connected, because this ensures that all solid/airflow interaction terms will be recognized, and consistent approximations or parameterisations can (ideally) be made.

In the case of a fence, the rate of extraction of momentum has been parameterised

$$\begin{aligned} \mathrm{SU} &= -k_{\mathrm{r}}\,\bar{u}|\bar{u}|\delta(x, 0)\,s(z,H) \\ \mathrm{SW} &= 0 \end{aligned} \tag{2}$$

where $k_{\mathrm{r}}$ is the "resistance coefficient" or "pressure loss coefficient" of the fence (see Laws and Livesey [10]; note that their definition of $k_{\mathrm{r}}$ contains a factor of 1/2 which is omitted herein), $\delta(x, 0)$ is the delta function (zero unless $x = 0$) having dimensions (length$^{-1}$) and $s(z,H)$ is a dimensionless unit step function defined by ($s = 1$ for $z \leqslant H$; $s = 0$ for $z > H$) where $H$ is the height of the fence. For vegetative shelter the momentum sink terms may be written as

$$\begin{aligned} \mathrm{SU} &= -c_{\mathrm{D}}(x, z)\,a(x, z)\,\bar{u}|\bar{u}| \\ \mathrm{SW} &= 0 \end{aligned}$$

where $a(x, z)$ is the leaf area density (dimensions, length$^{-1}$) and $c_{\mathrm{D}}$ is the corresponding drag coefficient. This parameterisation has been widely used to relate the wind profile within a horizontally uniform plant canopy to the within-canopy Reynolds stress divergence; see, for example, WS and Wilson et al. [11].

The parameterisation of porous shelter via the imposition of a momentum sink is both natural and convenient, and is superior to the treatment of

shelter by adding an extra boundary condition (see, for example, HSMK, who specified the velocity profile at the fence).

Rigorous budget equations for the turbulent stresses appearing in the momentum equations (1a, b) may be derived by manipulation of the Navier–Stokes equations. Again, careful attention to the averaging process is necessary to formally account for the interaction between the flow and immersed solids. Following RS, the stress budget equation for neutrally stratified steady flow is

$$\bar{u}_j \frac{\partial \overline{u_i' u_k'}}{\partial x_j} = -\overline{u_k' u_j'} \frac{\partial \bar{u}_i}{\partial x_j} - \overline{u_i' u_j'} \frac{\partial \bar{u}_k}{\partial x_j} \tag{3}$$

$$- \frac{\partial}{\partial x_j} \overline{u_i' u_k' u_j'} - \frac{1}{\rho} \frac{\partial \overline{u_k' p'}}{\partial x_i} + \frac{1}{\rho} \frac{\partial \overline{u_i' p'}}{\partial x_k} + \overline{\frac{\rho'}{\rho} \left( \frac{\partial u_k'}{\partial x_i} + \frac{\partial u_i'}{\partial x_k} \right)}$$

$$- 2\nu \overline{\frac{\partial u_i'}{\partial x_j} \frac{\partial u_k'}{\partial x_j}} + S_{ik}$$

Here $\nu$ is the kinetic viscosity, viscous diffusion has been dropped, and again the airflow/solid interaction terms have been "disguised" in $S_{ik}$.

By setting $i = k$ we may obtain the TKE budget equation for a two-dimensional flow

$$\frac{\partial}{\partial x}(\bar{u}\bar{e}) + \frac{\partial}{\partial z}(\bar{w}\bar{e}) = - \overline{u'^2} \frac{\partial \bar{u}}{\partial x} - \overline{w'^2} \frac{\partial \bar{w}}{\partial z} - \overline{u'w'} \left( \frac{\partial \bar{u}}{\partial z} + \frac{\partial \bar{w}}{\partial x} \right) \tag{4}$$

$$- \frac{\partial}{\partial x} \left( \overline{u'e} + \frac{1}{\rho} \overline{u'p'} \right) - \frac{\partial}{\partial z} \left( \overline{w'e} + \frac{1}{\rho} \overline{w'p'} \right)$$

$$- \epsilon + \mathrm{SE}$$

where $e = 1/2\, u_k' u_k'$.

Here it has been assumed that the scales of motion responsible for the energy dissipation are isotropic and the viscous dissipation term has been rewritten as

$$2\nu \overline{\frac{\partial u_i'}{\partial x_j} \frac{\partial u_k'}{\partial x_j}} = 2/3 \delta_{ik} \epsilon$$

$\epsilon$ is the rate of dissipation of turbulent kinetic energy, and $\mathrm{SE} = 1/2 S_{ii}$ represents conversion of mean flow kinetic energy into TKE of the wake flow. From the formal expressions for SU and $S_{ii}$ (see WS) it follows that if SU is parameterized as $-k_r \bar{u}|\bar{u}|\delta(x, 0)\, s(z,H)$ then $S_{ii} = + 2k_r \bar{u}^2 |\bar{u}| \delta(x, 0)\, s(z,H)$. However, as discussed in Section V it was found to be advantageous to simply set $S_{ik} = 0$ and all results to be shown were obtained with $S_{ik} = 0$ unless otherwise stated.

The reader may wonder how the spatially averaged flow variables which

appear in the governing equations may be compared with time-averaged single-point experimental data. RS have shown that, strictly, one may not consider the large area spatial average (their scheme I) and the small area spatial average + temporal average (their scheme II) to be equivalent. However, the terms which distinguish the budget equations under the two schemes have in any case been neglected in this work, and the numerical solutions have been compared with time-average observations.

## III. Closure schemes

The turbulent stress-gradient terms which appear in the mean flow equations (1a, b) as a result of the averaging process necessitate the adoption of closure relationships in order to obtain a closed set of equations. The closure scheme employed in numerical simulation of a turbulent flow problem is of crucial importance, and is likely to control the success (accuracy) of the simulation (note that eqns. 1, 3 and higher-order equations derived from the Navier—Stokes equations may be used interpretively without the need of closure hypotheses). As flow problems of increasing complexity have been addressed, there has been a corresponding increase in the complexity of the closure schemes adopted. However, recently, Hunt et al. [12], summarising the findings of a colloquium on air flow and dispersion in rough terrain, stated that "the current evidence is that it is not necessarily beneficial to use ever more complex models as the terrain becomes more complex".

In this investigation of flow through a windbreak, numerous closure schemes have been employed. All are well known, and will be briefly described and labelled for convenience of reference.

### *A. First-order closure*

The turbulent stresses are modelled as

$$\overline{u'w'} = -K\left(\frac{\partial \bar{u}}{\partial z} + \frac{\partial \bar{w}}{\partial x}\right) \tag{5a}$$

$$\overline{u'^2} = c_u\bar{e} - K\left(\frac{\partial \bar{u}}{\partial x} - \frac{\partial \bar{w}}{\partial z}\right) \tag{5b}$$

$$\overline{w'^2} = c_w\bar{e} + K\left(\frac{\partial \bar{u}}{\partial x} - \frac{\partial \bar{w}}{\partial z}\right) \tag{5c}$$

Here $K$ is the eddy viscosity, $\bar{e}$ the turbulent kinetic energy, $1/2\ \overline{u_i'u_i'}$, and $c_u$ and $c_w$ are constants. Unless otherwise stated the equilibrium values of the velocity variances were set at $\overline{u'^2} = (2.3u_{*0})^2$, $\overline{v'^2} = \overline{w'^2} = (1.3u_{*0})^2$.

#### *A1. Equilibrium eddy viscosity,* $K_0$

The eddy viscosity is held everywhere at its "equilibrium" or "far upstream" form

$$K_0(x,z) = ku_{*0}z \tag{6}$$

where $k$ is von Karman's constant ($k$ = 0.4 used herein), and $u_{*0}$ is the far-upstream friction velocity. The turbulent kinetic energy is held constant and thus $c_u$, $c_w$, $\bar{e}$ do not affect the solution (since only gradients in $\overline{u'^2}$, $\overline{w'^2}$ directly affect $\bar{u}$, $\bar{w}$ through the mean momentum equations).

*A2. Prandtl's eddy viscosity*, K—$P_r$

The eddy viscosity has been formed by the product of the equilibrium length scale $l_0 = kz$ and a local velocity scale derived from the mean shear $q = l_0\left|\frac{\partial \bar{u}}{\partial z}\right|$. Again, $\bar{e}$ was held fixed.

*A3. One-equation model*, K—$\bar{e}$

The eddy viscosity is formed by the product of the equilibrium length scale, $l_0$, and a velocity scale, $q = \sqrt{c\bar{e}}$, formed from the TKE. A budget equation for $\bar{e}$ is solved with the momentum equations. This TKE equation is eqn. (4) with the additional closure relationships

$$\overline{u'e} + \frac{1}{\rho}\overline{u'p'} = -K\frac{\partial \bar{e}}{\partial x} \tag{7a}$$

$$\overline{w'e} + \frac{1}{\rho}\overline{w'p'} = -K\frac{\partial \bar{e}}{\partial z} \tag{7b}$$

$$\epsilon = (c\bar{e})^{3/2}/kz \tag{7c}$$

$$c = u_{*0}^2/\bar{e}_0 \tag{7d}$$

The energy dissipation rate, $\epsilon$, is thus assumed to retain the same relationship to $\bar{e}$ as it does in the equilibrium surface layer (where shear production rate = dissipation rate). It is worth noting here that Finnigan and Bradley [6] concluded that the pressure and turbulent transport terms, replaced here by a gradient-diffusion expression, were of key importance in the TKE budget of their shelter flow.

*A4. Two-equation model*, K—$\bar{e}$—$\epsilon$ *(often called* k—$\epsilon$*)*

The eddy viscosity is written as $K = (c\bar{e})^2/\epsilon$ and equations are included for both $\bar{e}$ and $\epsilon$ (Launder and Spalding [13], LS). The $\bar{e}$ and $\epsilon$ equations used are exactly those given by LS (equations 2.2-1 and 2.2-2)

$$\frac{\partial}{\partial x}(\bar{u}\,\bar{e}) + \frac{\partial}{\partial z}(\bar{w}\,\bar{e}) = \frac{\partial}{\partial x}\left(K\frac{\partial \bar{e}}{\partial x}\right) + \frac{\partial}{\partial z}\left(K\frac{\partial \bar{e}}{\partial z}\right) + K\left[\left(\frac{\partial \bar{u}}{\partial z} + \frac{\partial \bar{w}}{\partial x}\right)^2 + 2\left\{\left(\frac{\partial \bar{u}}{\partial x}\right)^2 + \left(\frac{\partial \bar{w}}{\partial z}\right)^2\right\}\right] - \epsilon \tag{8}$$

$$\frac{\partial}{\partial x}(\bar{u}\epsilon) + \frac{\partial}{\partial z}(\bar{w}\,\epsilon) = \frac{\partial}{\partial x}\left(K/\sigma_\epsilon \frac{\partial \epsilon}{\partial x}\right) + \frac{\partial}{\partial z}\left(K/\sigma_\epsilon \frac{\partial \epsilon}{\partial z}\right)$$
$$+ C_{\epsilon 1}\,\epsilon/\bar{e}\,K\left[\left(\frac{\partial \bar{u}}{\partial z} + \frac{\partial \bar{w}}{\partial x}\right)^2 + 2\left\{\left(\frac{\partial \bar{u}}{\partial x}\right)^2 + \left(\frac{\partial \bar{w}}{\partial z}\right)^2\right\}\right] \qquad (9)$$
$$- C_{\epsilon 2}\,\epsilon^2/\bar{e}$$

The values of the constants were set as $C_{\epsilon 1} = 1.44$, $C_{\epsilon 2} = 1.92$, $\sigma_\epsilon = 1.3$ as recommended by LS. Equation (8) for TKE differs from that used with the $K - \bar{e}$ scheme only in the absence of the term $\bar{e}(c_u \frac{\partial \bar{u}}{\partial x} + c_w \frac{\partial \bar{w}}{\partial z})$.

*B. Second-order closure*

By including budget equations for the stresses, whose gradients appear in the mean momentum equations, one hopes to arrive at a mathematical model which is a more accurate description of reality than a gradient-diffusion closure scheme. The major difficulty is again closure: while some of the stress budget terms may be directly implemented in a model (e.g., transport by the mean flow, mean shear generation), others (turbulent and pressure transport, redistribution) must be related back to known quantities.

The second-order closure scheme introduced by Mellor [14] in a simulation of the horizontally uniform stratified surface layer was investigated for the windbreak problem, but the results were very discouraging. The second-order scheme used herein is one of several proposed and tested (in a variety of types of flow) by Launder et al. [15] (LRR). It was used by Pope and Whitelaw [16] (PW) to predict a number of wake flows. The model will here be labelled "LRR20C" (Pope and Whitelaw termed it Reynolds-stress model II). The closure hypotheses are

$$\overline{u_i' u_j' u_k'} = -c_s' \bar{e}/\epsilon\, \overline{u_k' u_l'}\, \frac{\overline{\partial\, u_i' u_j'}}{\partial x_l} \qquad (10)$$

$$\overline{\frac{p'}{\rho}\left(\frac{\partial u_i'}{\partial x_j} + \frac{\partial u_j'}{\partial x_i}\right)} = -c_1\,\epsilon/\bar{e}\,\left(\overline{u_i' u_j'} - \frac{2}{3}\,\bar{e}\,\delta_{ij}\right) - c_2\left(P_{ij} - \frac{2}{3}\,P\delta_{ij}\right) \qquad (11)$$

$$\frac{\partial}{\partial x_i}\,\overline{p' u_j'} + \frac{\partial}{\partial x_j}\,\overline{p' u_i'} = 0 \qquad (12)$$

$$\frac{\partial}{\partial x}(\bar{u}\,\epsilon) + \frac{\partial}{\partial z}(\bar{w}\,\epsilon) = \epsilon/\bar{e}\,\left(c_{\epsilon 1} P - c_{\epsilon 2}\,\epsilon\right) + c_\epsilon \frac{\partial}{\partial x_k}\left(\frac{\bar{e}}{\epsilon}\,\overline{u_k' u_l'}\,\frac{\partial \epsilon}{\partial x_l}\right) \qquad (13)$$

where

$$P_{ij} = -\overline{u_i' u_k'}\,\frac{\partial \bar{u}_j}{\partial x_k} - \overline{u_j' u_k'}\,\frac{\partial \bar{u}_i}{\partial x_k} \qquad (14)$$

and

$$P = -\overline{u_i' u_j'} \frac{\partial \bar{u}_i}{\partial x_j} \tag{15}$$

No near-wall correction to the pressure strain is included. Note that eqn. (13) is simply a generalisation of the dissipation equation used with the "$k$—$\epsilon$" model (eqn. 9). The velocity triple-correlation equation is a simple gradient-diffusion hypothesis, and as pointed out by LRR it does not behave properly under a rotation of the dummy indices.

On the assumption of an equilibrium neutral surface layer (advection = diffusion = 0; TKE production rate = dissipation rate; height-independent $\overline{u'w'}$, $\overline{u'^2}$, $\overline{v'^2}$, $\overline{w'^2}$; logarithmic velocity profile) the LRR Reynolds-stress

TABLE 1

Values of arbitrary constants arising in the second-order closure scheme of Launder et al. [15]

| Constant | Present work | Previous work | |
|---|---|---|---|
| | | LRR | PW |
| $C_1$ | 2.114 | 1.5 | 2.5 |
| $C_2$ | 0.6 | 0.6 | 0.4 |
| $C_s'$ | 0.25 | 0.25 | 0.25 |
| $C_{\epsilon 1}$ | 1.45 | 1.44 | 1.45 |
| $C_{\epsilon 2}$ | 1.90 | 1.90 | 1.90 |
| $C_\epsilon$ | 0.17 | 0.15 | 0.15 |
| $\overline{u'^2}/u_{*0}^2$ | 2.87 | | |
| $\overline{v'^2}/u_{*0}^2 = \overline{w'^2}/u_{*0}^2$ | 1.69 | | |
| $\bar{e}/u_{*0}^2$ | 3.13 | | |

equations reduce to a set of algebraic equations which determine the stresses given values of the arbitrary constants. Table 1 gives the values used herein for the constants. The rationale for the choices made was to follow the suggestion of LRR as closely as possible but to impose the condition (well obeyed in the neutral atmospheric surface layer) that $\overline{w'^2}/u_{*0}^2 \approx 1.3^2$.

## IV. Numerical method

The early stages of this work used a vorticity-stream function formulation or a primitive equation formulation using Chorin's method of artificial compressibility. Much time was wasted combatting numerical instability. It was a relief to be introduced to the SIMPLE method, which is very clearly described by Patankar [17] (PAT), one of its developers. An understanding of SIMPLE may be quickly gained by reading PAT and only a brief outline will be given here.

The equations to be solved are cast in a standard form which will be illustrated using the $\bar{u}$-mtm equation

$$\frac{\partial}{\partial x}\left(\bar{u}\,\bar{u} - K\frac{\partial \bar{u}}{\partial x}\right) + \frac{\partial}{\partial z}\left(\bar{w}\,\bar{u} - K\frac{\partial \bar{u}}{\partial z}\right)$$

$$= -\frac{1}{\rho}\frac{\partial \bar{p}}{\partial x} - \frac{\partial \overline{u'^2}}{\partial x} - \frac{\partial \overline{u'w'}}{\partial z} - k_r\,\bar{u}|\bar{u}|\delta(x,0)\,s(z,H) \qquad (16)$$

$$-\frac{\partial}{\partial x}\left(K\frac{\partial \bar{u}}{\partial x}\right) - \frac{\partial}{\partial z}\left(K\frac{\partial \bar{u}}{\partial z}\right)$$

Here the diffusion terms added on the left-hand side have also been added on the right-hand side, so that this is exactly eqn. (1a). With first-order closure schemes the parameterisation for $\overline{u'^2}$, $\overline{u'w'}$ wipes out the diffusion terms on the right-hand side. In the case of second-order closure, all the diffusion terms in the $\bar{u}$-mtm equation as written above are fictitious, but cancel.

The next step in SIMPLE is to split up the space into finite control volumes and integrate the equations within their respective control volumes to obtain equations which state that flux differences across sides of the control volume must balance the source enclosed (as Patankar calls it, a "pre-calculus" expression of conservation). Thus

$$J_E - J_W + J_N - J_S = \mathrm{SU}\Delta x\Delta z$$

where $J$ is the (advective plus diffusive) flux of $\bar{u}$-momentum across control volume faces (labelled $E$, $W$, $N$, $S$). One component of the source term will be $-k_r\bar{u}|\bar{u}|\Delta z \int_W^E \delta(x,0)\mathrm{d}x$ which vanishes except for control volumes which cross $x = 0$. It is very convenient that, using SIMPLE, the $\delta$ function is replaced by its integral.

The continuity equation is next integrated throughout the control volume, multiplied by the grid point value of the variable in question (here $\bar{u}$), and subtracted from the conservation equation. One finally obtains linearised discretization equations of the form

$$a_c\,u_c = a_e\,u_e + a_w\,u_w + a_n\,u_n + a_s\,u_s + b + \text{pressure term}$$

where the neighbour coefficients ($a_c$, $a_e$, etc.) depend on the current best estimate of the unknown fields. Patankar gives a set of simple rules for evaluating the coefficients which ensures accurate conservation and numerical stability. Further details follow.

*1. Grid*

The SIMPLE method solves the $\bar{u}$-mtm, $\bar{w}$-mtm, and continuity equations at staggered points in space (see Fig. 1). The control volumes were here set up by first specifying the locations of the $\bar{u}$ (■) and $\bar{w}$ (●) points (through which pass the control volume boundaries for the pressure correction equa-

tion) then placing the pressure points (○) at the centre of the control volume thus defined.

The boundaries of the computational domain run through points at which the boundary-normal velocities are defined. Consequently, there are no incomplete $\bar{u}$-control volumes adjacent to the top and bottom boundaries, and no boundary condition on $\bar{u}$ is needed at these boundaries. However, one must specify values of the momentum flux to/from $\bar{u}$-control volumes at the top and bottom boundaries.

*2. Boundary conditions*

*(a) Horizontal velocity*

$\bar{u}$ was specified at the upstream edge $\bar{u} = \bar{u}_0(z)$ and at the outflow the condition $\dfrac{\partial \bar{u}}{\partial x} = 0$ was imposed ($\bar{u}$ $(IHI, J) = \bar{u}$ $(IHI - 1, J)$ where $I$ and $J$ label the horizontal and vertical axes of the grid).

*(b) Vertical velocity*

Specified as $\bar{w} = 0$ at the top and bottom computational boundaries. At the side boundaries a zero-lateral-flux (of vertical momentum) condition was imposed.

*(c) Pressure*

As discussed by PAT and by Van Dormal and Raithby [18] (VDR), with

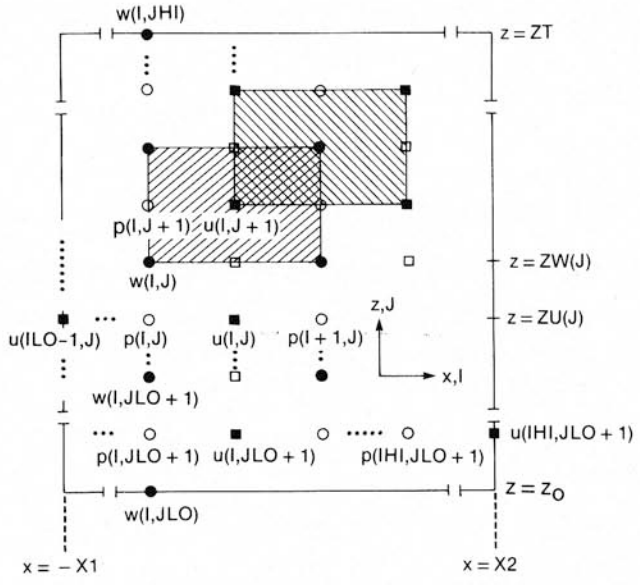


Fig. 1. Schematic diagram of the staggered grid. Spacings shown as uniform for simplicity. Pressure grid points (○), $\bar{u}$ grid points (▪), $\bar{w}$ grid points (•). $\bar{u}$ control volume denoted▨, $\bar{w}$ control volume denoted▧.

the above boundary conditions on the mean velocities no arbitrary specification of pressure boundary conditions is necessary.

*(d) Stresses* ($\overline{u'^2}$, $\overline{v'^2}$, $\overline{w'^2}$, $\overline{u'w'}$)

In the second-order closure formulation the stresses were placed at the points marked (□) on the grid. This choice enables direct determination (without interpolation) of the important shear production terms (involving $\partial\bar{u}/\partial z$) of the stress budget equations and the stress gradients appearing in the momentum equations. Furthermore, the outermost stress gridpoints then lie on the computational boundaries, so from all points of view this choice seems the natural one.

The stresses were directly specified on the upstream and top boundaries as

$$\overline{u'^2} = a_u u_{*0}^2 \qquad \overline{v'^2} = a_v u_{*0}^2 \qquad \overline{w'^2} = a_w u_{*0}^2 \qquad \overline{u'w'} = -u_{*0}^2 \tag{17}$$

At the ground, a local friction velocity was formed from the lowest-defined $\bar{u}$-velocity

$$u_*(I) = \frac{k\,\bar{u}_p}{\ln(z_p/z_0)} \tag{18}$$

where subscript $p$ indicates height $ZU(JLO+1)$. This friction velocity then determined the momentum flux to ground, and, via the assumption of a local equilibrium layer, the surface values of $\overline{u'^2}$, $\overline{v'^2}$, $\overline{w'^2}$ using the equilibrium relationships $\overline{u'^2} = a_u u_*^2(I)$, etc. This stress lower-boundary condition is further discussed in Section V.

At the downstream boundary, $\dfrac{\partial}{\partial x} = 0$ was imposed.

*(e) TKE and dissipation*

Under the $K$—$\bar{e}$ scheme, TKE was placed at the (□) points. TKE was then specified upwind and along the top boundary, while at the ground $\dfrac{\partial}{\partial z} = 0$ was imposed and downstream $\partial/\partial x = 0$ was imposed. As well as obtaining the surface momentum flux (required as a boundary condition for the $\bar{u}$-mtm equation) by eqn. (18), as an alternative the "wall function"

$$u_*^2(I) = \left[\frac{k\bar{u}_p}{\ln(z_p/z_0)}\right] \sqrt{c\,\bar{e}\,(I, JLO)} \tag{19}$$

suggested by LS was used. These two alternatives will henceforth be distinguished as $u_* = u_*(\bar{u})$, $u_* = u_*(\bar{u}, \bar{e})$.

For the $K$—$\bar{e}$—$\epsilon$ scheme the energy and dissipation were placed either at the conventional location (○), or at the points (□) of Fig. 1 where the key velocity-gradient source terms are directly available. The outcome of predictions was much more sensitive to the treatment of the lower boundaries than

to the choice of location of $\bar{e}$, $\epsilon$, and because the (□) location is more convenient (direct specification of $\bar{e}$, $\epsilon$ upstream and at the lid rather than flux specifications, and simpler evaluation of source terms) all results shown here use the (□) positioning. The lower boundary was treated thus: the vertical gradient of $\bar{e}$ was set to zero at ground, and the value of $u_*$ (either $u_*(\bar{u})$ or $u_*(\bar{u}, \bar{e})$) was taken to fix $\epsilon$ both at $z_0$ ($J = JLO$) and at $J = JLO + 1$, assuming near-ground height variation as $u_*{}^3/kz$.

For convenience the domain used will be denoted

$$D = [X1/H{:}X2/H,\ ZT/H]^{NZL}_{NXLUW,\ NXLDW}$$

where $X1$ = inflow boundary, $X2$ = outflow boundary, $ZT$ = top boundary, $NZL$ = number of rows, $NXLUW$ = number of columns upwind, $NXLDW$ = number of columns downwind.

*3. Stretching of grid*

In order to obtain the field of species $\phi$ (which could be momentum), SIMPLE actually solves conservation equations which contain an extra term $(\nabla \cdot \bar{\mathbf{u}})_p\ \phi_p$ where subscript $p$ indicates the divergence is estimated at the $\phi$-gridpoint $p$. Although SIMPLE ensures that $\nabla \cdot \bar{\mathbf{u}}$ is very small at pressure gridpoints, the divergence at other points is not necessarily of similar (negligible) size unless the grid volume dimensions are position-independent.

In this work it is highly desirable to focus computational effort near the windbreak, but to ensure that this "continuity violation term" (CVT) is unimportant the control volume dimensions have never varied by more than 20% between adjacent control volumes (this precludes use of a logarithmic grid). The volume-integrated continuity violation term has been monitored to ensure it is small (<2%) with respect to the drag on the windbreak.

The horizontal spacing followed the series

$$\frac{xu}{H} = 0,\ 2,\ 2 + (1.2 \times 2) = 4.4,\ 4.4 + (1.2 \times 2.4) \ldots$$

and the vertical spacing used was

$$\frac{zw}{H} = \frac{z_0}{H},\ 0.25,\ 0.5,\ 0.75,\ 1.0,\ 1.0 + (1.2 \times 0.25) = 1.30 \ldots *$$

---

*Note added in proof. The sensitivity of the numerical solutions to changes in the resolution (as distinct from domain size) was not systematically investigated. It has since been found that improved resolution yields changes in the solutions which are not insignificant. Solutions given here must not be regarded as grid-independent. No clear pattern to the changes caused by altering the grid resolution has been established, and it has proven impossible to demonstrate grid-independence even with a computational effort amounting to 2 h of CPU time. Durst and Rastogi [3] experienced this problem in their simulation of separating flow past a solid fence. Where the findings of this paper are cast in doubt by the grid-dependence problem a footnote to that effect will be given.

*4. Non-dimensionalisation*

All velocities were normalised by $u_{*0}$, all lengths by $z_0$.

*5. Advection/diffusion scheme*

All work reported used Patankar's power-law scheme (see PAT).

*6. Pressure-correction equation*

Rather than the method given by PAT, the revision called SIMPLEC and described by Van Doormal and Raithby [18] has been employed.

*7. Solution of the discretization equations*

The discretization equations have been solved using a line-by-line solver (successive passes of a tridiagonal matrix solver in alternate directions) with repetitions continued until the square root of the sum of the squares of residuals is reduced by an arbitrary factor (usually 1/4) (see PAT and VDR).

*8. Force balance: a test for convergence and accuracy*

Analytical integration of eqn. (1a) (conservation of $\bar{u}$-momentum) between limits $\int_{X1}^{X2} \int_{z_0}^{ZT}$ where $ZT$ is sufficiently high that $\bar{w}(ZT) = 0$ yields

$$\left[\bar{u}^2 + \overline{u'^2} + \frac{\bar{p}}{\rho}\right]_{X1}^{X2} + [\overline{u'w'}]_{z_0}^{ZT} + \mathrm{FD} = 0 \tag{20}$$

where FD is the total drag on the fence per unit crosswind length.

Using the SIMPLE method the continuity violation term, CVT, mentioned earlier must also be included in the force balance. After each cycle (consisting of definition of new neighbour coefficients and solution of the resulting equations) the terms in the force balance equation were evaluated. Iterations ceased when the force balance (including CVT which was itself small) was correct to within 1% of the total drag, FD, and all individual residuals at each grid point for each variable were smaller than a specified limit. This normally required about 100 ± 20 cycles. Using single precision on an IBM 3081D, solutions using second-order closure required about 5 CPU minutes. Checks on the mass balance indicated inflow = outflow to about 8 significant figures.

*9. Smoothing and relaxation*

No supplementary smoothing was used. In most cases the equations contain diffusion (smoothing) terms as a consequence of closure hypotheses. In the case of the $\bar{u}$- and $\bar{w}$-momentum equations under second-order closure this is not the case; it should be noted that the diffusion terms (employing eddy viscosity, $K_0$) added to the left- and right-hand sides of these equations (to obtain the standard SIMPLE form) cancel.

It was found necessary to provide heavy relaxation ($E$ = 0.5 in the ter-

minology of van Doormaal and Raithby) to ensure numerical stability when using second-order closure. This relaxation affects the rate of progress towards, but not the accuracy of, the final solution.

*10. Equilibrium consistency*

In every case the numerical model retained the imposed inflow-boundary equilibrium values of all variables with a high degree of accuracy when allowed to run without the momentum sink corresponding to the fence.

## V. Comparison of predictions with experimental data

The closure schemes described in Section III have been used to predict the flow pattern for a fence corresponding to that used in the experiment described by Bradley and Mulhearn [7] and Finnigan and Bradley [6].

A section of fence corresponding to the description of Bradley and Mulhearn (vertical slats of wood, 1.2 × 0.08 × 0.01 m, 50% porosity) was built and placed in a wind tunnel so as to block the tunnel (as mounted in the tunnel, the porosity was 0.48). The resistance coefficient of the fence was determined by measuring the pressure difference across the fence (1.5 m upstream to 3 m downstream) and dividing by $\rho\bar{u}^2$ where $\bar{u}$ is the measured tunnel windspeed (note that the resistance coefficient is commonly defined as $k_r = \Delta p/(1/2\ \rho u^2)$; the factor 1/2 has been omitted from the definition herein). Eight measurements with 1.5 m s$^{-1}$ $\leqslant \bar{u} \leqslant$ 6 m s$^{-1}$ yielded $k_r = 1.97$ (sample standard deviation 0.04) with no obvious speed-dependence. This is in good agreement with a formula given by Hoerner [19] which, for a sharp-edged fence of porosity 50%, predicts $k_r = 2$. Baines and Peterson [20] gave a graph summarising resistance coefficients as a function of porosity which indicates a value of about 1.6 for "square bar lattices". Unless stated otherwise, simulations used $k_r = 2.0$ and $z_0 = 0.002$ m ($H/z_0 = 600$).

The upstream equilibrium values, $\overline{u'^2}/u_{*0}^2$, $\overline{v'^2}/u_{*0}^2$, used in the numerical simulations fall within the range of values observed for atmospheric surface-layer flow, but they do not necessarily precisely match the Bradley and Mulhearn experiments. It has been found that the predicted mean velocity fields are rather insensitive to the equilibrium values incorporated for $\overline{u'^2}$, $\overline{v'^2}$. Furthermore, since the numerical models contain only a single turbulence timescale, $\bar{e}/\epsilon$, one cannot hope to match in detail the manner in which a real wake flow might respond to changes in the approach spectra (due, for example, to changes in the $\overline{u'^2}$ spectrum caused by variations in planetary boundary layer depth). One can only hope that such responses are in reality of secondary importance. That this is so is indirectly indicated by the experimental data; results obtained on different occasions could be cast in a universal form by a very simple normalisation (division by a reference upstream mean velocity).

*A. Mean flow, pressure*

Figure 2 shows the observed vertical profile of normalised horizontal windspeed, $\bar{u}/\bar{u}_{04}$ (where $\bar{u}_{04}$ is the average windspeed at $z$ = 4 m far upstream), at a downwind distance $x/H$ = 4.2. Also shown are the predictions of the $K_0$ scheme, for three sizes of the computational domain. Evidently, care must be taken that the "lid" is not too low; as the lid is raised the speedup over the fence declines (giving poorer agreement with observation in this case). Because the lid is impermeable, any deficit in mass flow rate in the lee of the shelter must be compensated by a surplus elsewhere. Hence, with the higher lid, the less intense speed-up must persist over a greater depth.

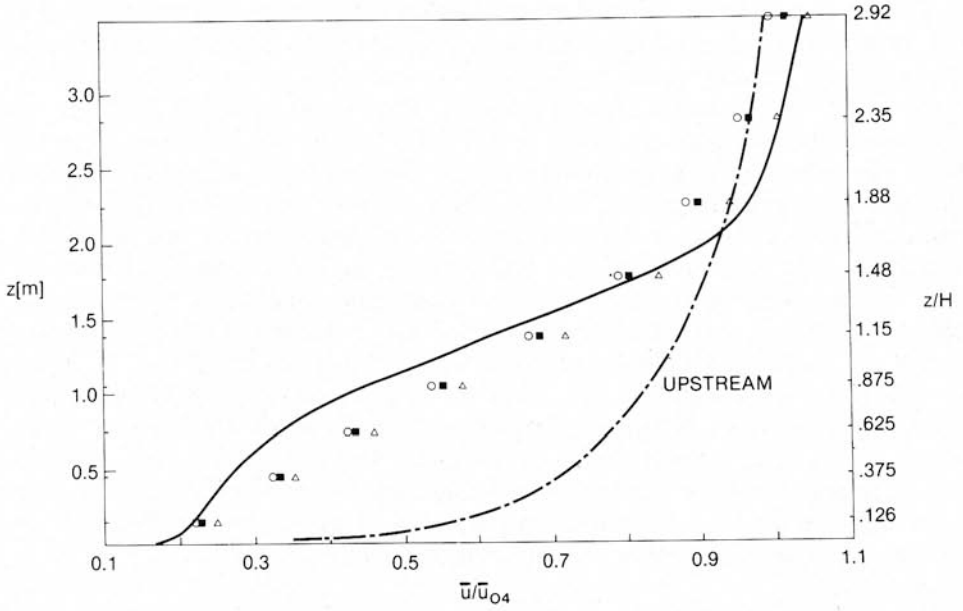


Fig. 2. Vertical profiles of $\bar{u}/\bar{u}_{04}$ at $x/H$ = 4.2 according to the $K_0$ scheme for several sizes of the computational domain: observations (——); upstream profile (— · —); (○) $D = [-60{:}112, 47]^{24}_{10,13}$; (■) $D = [-60{:}112, 16]^{18}_{10,13}$; (△) $D = [-60{:}60, 7]^{14}_{10,10}$.

When the domain size was increased from

$$D_s = [-60{:}112, 47]^{24}_{10,13} \text{ to } D = [-112{:}170, 82]^{27}_{13,15}$$

the largest changes in the solution were less than 1%. Therefore, $D_s$ has been used as the standard domain, and all results given used $D_s$ unless otherwise stated.

Figure 3 compares the predicted vertical profiles of $\bar{u}/\bar{u}_{04}$ at $x/H$ = 4.2 obtained with $D = [-60{:}60, 7.2]^{14}_{10,10}$ using $K_0$, $K$—$P_r$, and $K$—$\bar{e}$. Though it has been shown that this domain is insufficiently large, it may nevertheless be concluded that $K$—$P_r$ and $K$—$\bar{e}$ compare less favourably with the experimental data than does $K_0$. The $K$—$\bar{e}$ prediction shown used the wall function

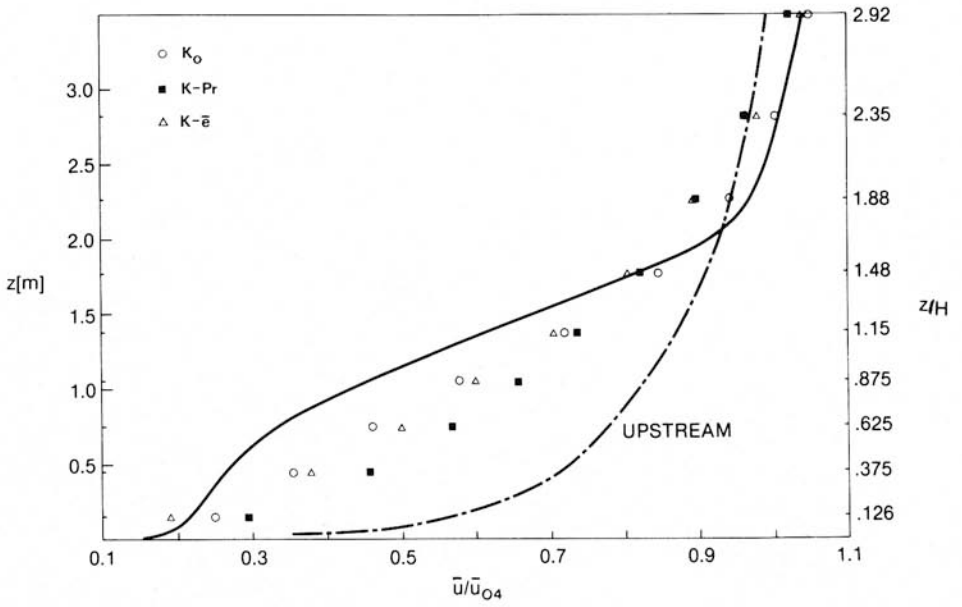


Fig. 3. Vertical profile of $\bar{u}/\bar{u}_{04}$ at $x/H = 4.2$ according to $K_0$ (○). $K$—$P_r$ (■), and $K$—$\bar{e}$ (△): observations (——); far upstream profile (— · —).

$u_* = u_* (\bar{u}, \bar{e})$. The $K$—$\bar{e}$ prediction using $u_*(\bar{u})$ differed noticeably only in the lowest 3 levels.

Below about $0.5H$, the shear, $\partial\bar{u}/\partial z$, in the lee of the windbreak is much weaker than $\partial\bar{u}_0/\partial z$, while over a range of $\sim 0.6$—$2H$ the opposite is the case. Thus, the Prandtl eddy viscosity behaves as

$K < K_0 \qquad z/H \lesssim 0.5$
$K > K_0 \qquad 0.6 \lesssim z/H \lesssim 2$

Precisely the opposite modification of $K$ with respect to $K_0$ is needed to "curve-fit" the prediction to the observations in the near lee of the windbreak; better agreement results from using a constant $K$ for $z < \sim 2H$ and then allowing an increase with height at the "normal" rate. Thus, the local shear (at least combined with length scale $kz$) is a poor predictor of the necessary velocity scale.

Figure 4 compares the $K$—$\bar{e}$—$\epsilon$ model (with $u_*(\bar{u}, \bar{e})$) and the $K_0$ model using the standard domain $D_s$. Over a range of heights around $z = H$ the $K$—$\bar{e}$—$\epsilon$ prediction is superior to $K_0$, but both share the failure to predict the distinct speedup observed. Also shown is the prediction of the $K$—$\bar{e}$—$\epsilon$ model with an extra term $-k_r u'^2\ \delta(x, 0)\ s(z,H)$ included in the $\bar{u}$-momentum source term SU. This term represents an additional momentum loss through the velocity fluctuations, and as the figure shows, has little effect at large heights where $\bar{u}^2 \gg u'^2$. Near the ground the term has a significant effect, but in view of the relatively large errors (with respect to the experimental data) above about $1.5H$ its inclusion is hardly warranted.

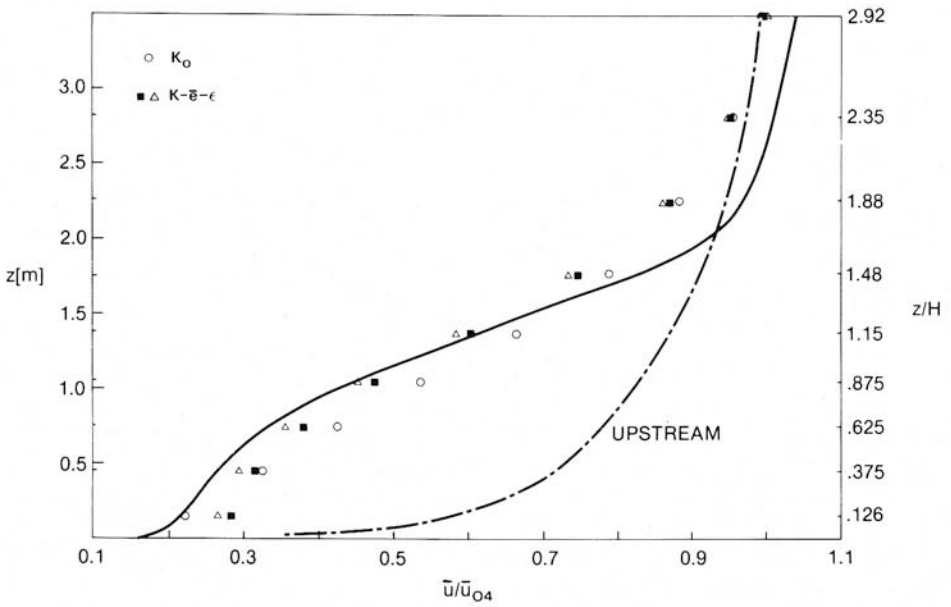


Fig. 4. Vertical profile of $\bar{u}/\bar{u}_{04}$ at $x/H = 4.2$ according to $K_0$, $K$—$\bar{e}$—$\epsilon$: observations (— - —); upstream profile (— · —); (○) $K_0$; (■) $K$—$\bar{e}$—$\epsilon$; (△) $K$—$\bar{e}$—$\epsilon$ with additional momentum sink term $+2k_r\overline{u'^2}|\bar{u}|\delta(x, 0)\, s(z,H)$.

Figure 5 compares the predicted profile of eddy viscosity $K = (c\ \bar{e})^2/\epsilon$ at $x/H = 4.4$ with the equilibrium profile $K_0 = 0.4u_{*0}z$. There is an interesting similarity to the commonly assumed variation of eddy diffusivity in and above a uniform canopy, with, in this case, an effective displacement height of order $H$. The region where $K$—$\bar{e}$—$\epsilon$ has yielded greatest improvement over $K_0$ is $\sim 0.5H - 2H$, the zone of approximately constant $K$ according to $K$—$\bar{e}$—$\epsilon$. The near-ground peak in $K$ was caused by small values of $\epsilon$ (relative to $\epsilon_0$) occurring near ground in the near lee of the fence. The values obtained for $K$ in this region (near ground at small $x/H$) depended strongly on the treatment at the lower boundary (choice of $u_*$, etc.) but above about $0.5H$ all $K$—$\bar{e}$—$\epsilon$ simulations showed the same features in the eddy viscosity profile.

Figure 6 compares the observed vertical profile of $\bar{u}/\bar{u}_{04}$ at $x/H = 4.2$ with that predicted by the LRR20C model. The $K_0$ and $K$—$\bar{e}$—$\epsilon$ (using $\bar{u}_*(\bar{u}, e)$) predictions are also shown. The agreement with experiment is, overall, slightly better than is obtained with the $K_0$ or $K$—$\bar{e}$—$\epsilon$ models, though again the speed-up over the top of the fence is not correctly predicted. Inclusion of a near-wall correction to the pressure—strain terms following the method of Gibson and Launder [21] yielded a mean velocity field negligibly different from that of LRR20C.

There was a very slight deterioration in the solution for the mean velocity when, as is consistent with the assignment $SU = -k_r\bar{u}|\bar{u}|\delta(x, 0)\, s(z,H)$, source

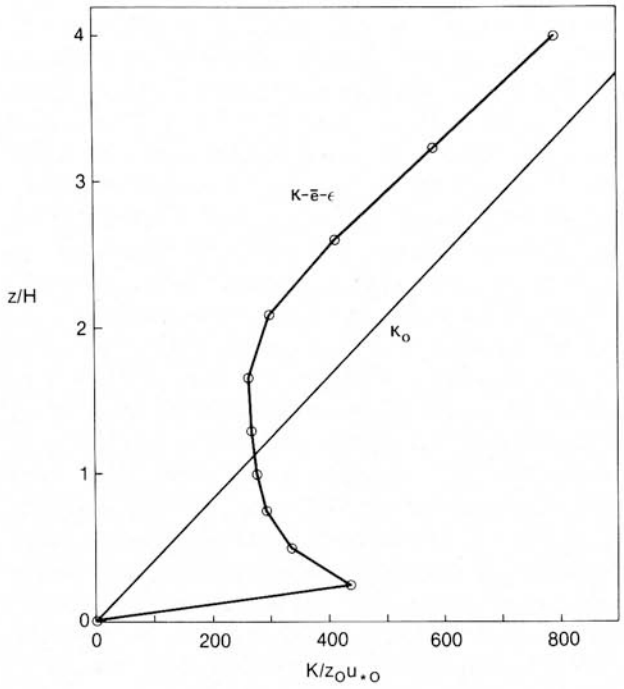


Fig. 5. Vertical profile of eddy viscosity at $x/H = 4.2$ according to the $K$—$\bar{e}$—$\epsilon$ scheme (—o—) and equilibrium profile (——).

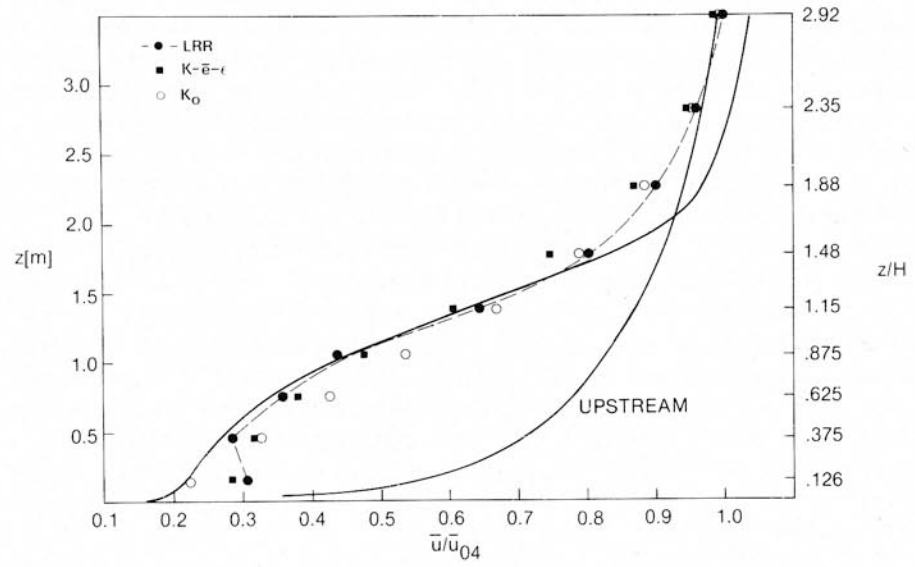


Fig. 6. Vertical profile of $\bar{u}/\bar{u}_{04}$ at $x/H = 4.2$ according to LRR20C (— • —), $K$—$\bar{e}$- (■), and $K_0$ (○).

terms + $2k_r\bar{u}^2|\bar{u}|\delta(x, 0)\, s(z,H)$ and + $k_r\bar{u}\bar{w}|\bar{u}|\delta(x, 0)\, s(z,H)$ were added to the $\overline{u'^2}$ and $\overline{u'w'}$ budget equations, respectively. The inclusion of these terms caused a large increase in the $\overline{u'^2}$ levels near the fence (virtually a step change in $\overline{u'^2}$ from a near equilibrium value to $\sim 13\ (\overline{u'^2})_0$ at $x/H = 0$, $z/H = 1$) but fairly modest changes to the $\overline{u'w'}$ field. It is quite possible that inclusion of these terms implies, to be consistent, the inclusion of extra terms elsewhere (e.g., in the energy dissipation equation; inclusion of the MKE → TKE term in the production term of the $\epsilon$ equation has lead to numerical instability which has not yet been overcome). As discussed later, increased TKE in the immediate lee of the fence is contrary to observation. In view of this, and because the changes to the mean field were fairly small and showed no impact on the overall problem of improving the prediction of the speed-up over the fence, it was decided to omit these source terms.

Over the range $4.4 \leqslant x/H \leqslant 15$ LRR20C predicted that the near ground speed $\bar{u}_p$ slightly exceeds the speed at the next higher gridpoint. This leads one to suspect that the lower boundary condition used for the stresses is not completely satisfactory. When the ground-level stresses were instead calculated from the normal budget equations expressed on the 1/2-control volume adjacent to the ground (neglecting stress-diffusion to ground and evaluating $\partial\bar{u}/\partial z$ from $\bar{u}_p$ on the assumption of a logarithmic profile) the predictions were negligibly altered, which implies that the mean flow and turbulent transport terms are, adjacent to the ground, of so little importance that in effect an equilibrium layer does exist; consequently, eqn. (17) is valid. Alternative methods which postulate a near-wall wind profile which is sensitive to the pressure gradient have been suggested. However, when the wall function corresponding to the suggestion of Rastogi and Rodi [22] was incorporated, the near-ground discrepancy was slightly worsened. The discrepancy at the ground is in any case of minor importance (though it may have a serious impact on the overall force balances to be presented) since alternative boundary treatments have been found to have very little impact on the solution except at the lowest $\bar{u}$-gridpoint, and the most serious problem is the failure to correctly predict the speed-up zone aloft.

Figure 7 shows the observed horizontal profile of $\bar{u}/\bar{u}_{04}$ at fixed heights $z/H = 0.4$, 1.9 and the corresponding predictions of the $K_0$, $K$—$\bar{e}$—$\epsilon$, and LRR20C models. The predictions give a rate of recovery towards the upstream (equilibrium) condition which is lower than that observed, and this is probably a consequence of the models' failure to predict the speed-up over the fence. It is of interest that the predictions of Pope and Whitelaw [16], for flow past a disk mounted perpendicular to an approaching airstream, show similar features: failure to predict the distinct speed-up in the outer layer (their fig. 10b) and underprediction of the rate of recovery towards upstream conditions (their fig. 9a).

Figure 8 gives the observed vertical profiles of $\bar{u}/\bar{u}_{04}$ at $x/H = 12.5$, 16.7 and the predictions at $x/H = 15.0$ of $K_0$, $K$—$\bar{e}$—$\epsilon$ and LRR20C. Again, at large heights all three numerical solutions fail to predict the observed speed-up.

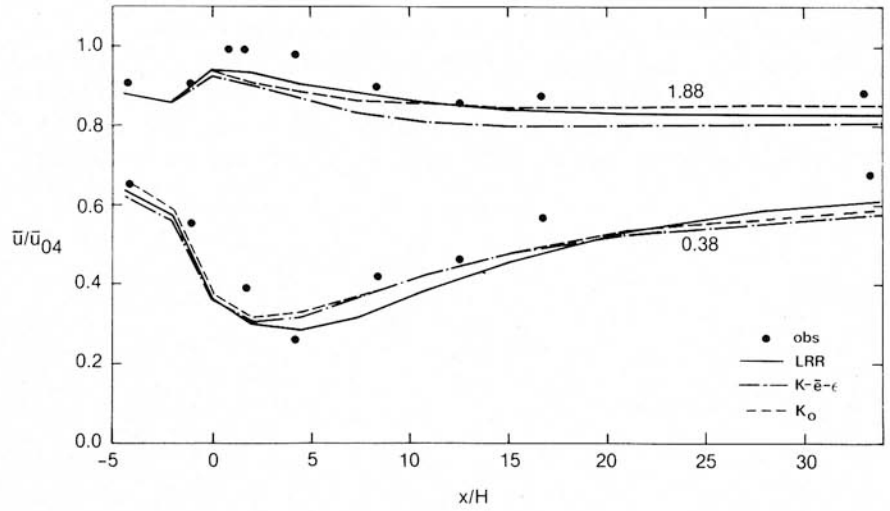


Fig. 7. Horizontal profiles of $\bar{u}/\bar{u}_{04}$ at $z/H$ = 0.38, 1.88. Observations (•), LRR20C (——), $K$—$\bar{e}$—$\epsilon$ (— · —), $K_0$ (— — —).

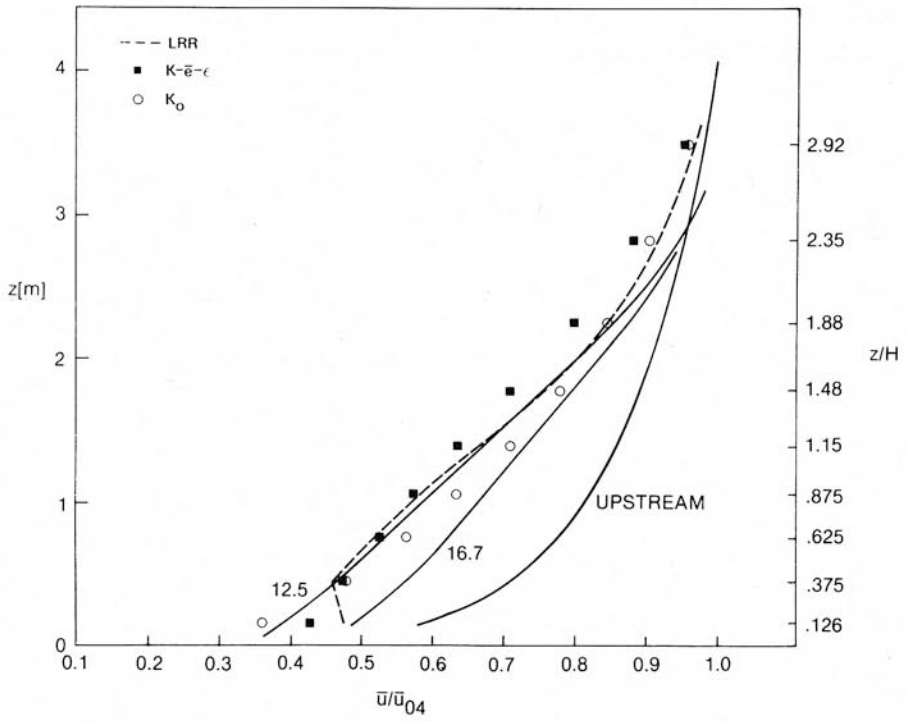


Fig. 8. Vertical profile of $\bar{u}/\bar{u}_{04}$ at $x/H$ = 15 according to LRR20C (— — —), $K$—$\bar{e}$—$\epsilon$ (▪), and $K_0$ (○). Observations upstream and at $x/H$ = 12.5, 16.7 (——).

Figures 9 and 10 indicate the sensitivity of the predictions using the LRR20C closure scheme to changes in the pressure loss coefficient, $k_r$. In Fig. 10, a plot of the relative slow-down $\Delta\bar{u}(z)/\bar{u}_{04}$ at $x/H = 4.2$, the profile for $k_r = 2.0$ shows very satisfactory agreement with observation below about $1.5H$ (i.e., in the most important region, for practical purposes). Tinkering with the value of $k_r$ yields no improvement in the pre-

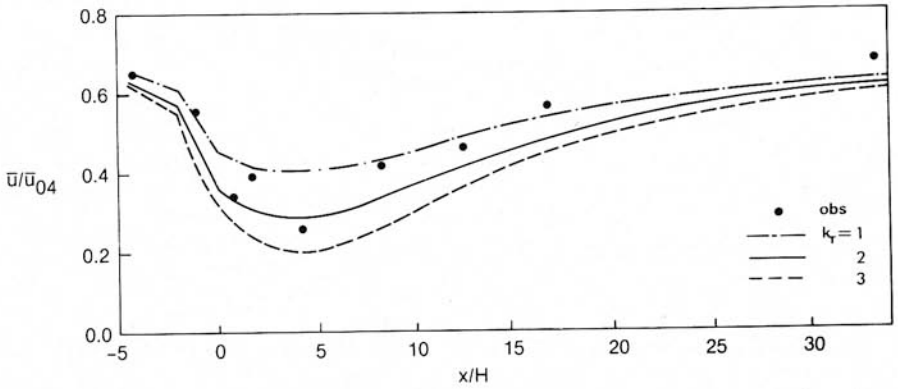


Fig. 9. Horizontal profiles of $\bar{u}/\bar{u}_{04}$ at $z/H = 0.38$ according to the LRR20C scheme with several values of the momentum loss coefficient. Observations (•).

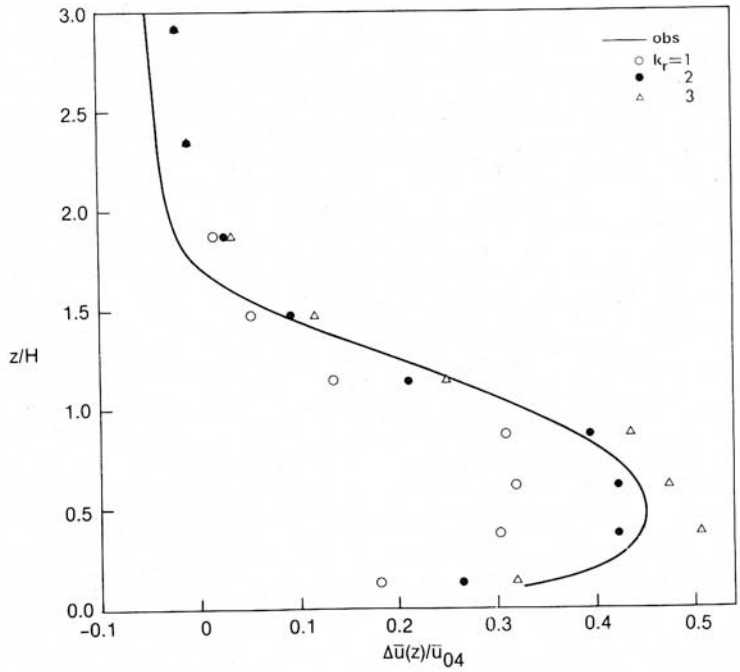


Fig. 10. Vertical profile of $\Delta\bar{u}/\bar{u}_{04}$ at $x/H = 4.2$ according to the LRR20C scheme for several values of the momentum loss coefficient $k_r$. Observations (——).

diction of the speed-up over the fence (and these are fairly large changes, corresponding to a range in porosity of about 62% through 50% to about 44%) which to some extent confirms that it is not an inadequacy of the parameterisation $-k_r\bar{u}|\bar{u}|\delta(x, 0)\, s(z,H)$ for the momentum sink which is responsible for the failings of the numerical model.

It is of interest to note from Fig. 9 that a larger value of $k_r$ leads to reduced windspeeds at all $x/H$, at least at $z/H = 0.38$. This is in contrast to the widely held belief that although a less permeable fence causes a deeper minimum in the horizontal profile of velocity, the rate of recovery to upstream conditions is more rapid, and, in consequence, little is gained by decreasing the porosity [23]. Table 2 summarises experimental findings on the effect of windbreak porosity on the rate of recovery towards the upstream equilibrium condition. These observations unambiguously indicate increasing downstream extent of wind reduction as the porosity is decreased, in agreement with the prediction of the numerical model.

Figure 11 shows a horizontal profile of vertical velocity predicted by the LRR20C scheme (those predicted by $K$—$\bar{e}$—$\epsilon$ and $K_0$ are almost identical. According to $K_0$, $K$—$\bar{e}$—$\epsilon$, and LRR20C the maximum updraft ($\bar{w} = 2.2\, u_{*0}$ at $x/H = -1$, $z/H = 1.3$) considerably exceeds the maximum downdraft ($\bar{w} = -0.30u_{*0}$ at $x/H = 9$, $z/H = 1.3$). The location of these peaks agrees well with the observations of Maki and Kawashima [26] (MK) for flow through a cheesecloth net. The upstream peak is of magnitude comparable to that observed by MK, but the downdraft is weaker than observed. The streamline inclination corresponding to the peak updraft is $\tan^{-1}\bar{w}/\bar{u} = 8.1°$; Finnigan and Bradley observed a maximum inclination of 6°. The "calibration condition" for the determination of the pressure-loss coefficient, $k_r$,

TABLE 2

Summary of observed dependence of the leeward extent of windspeed reduction (at $z/H = 0.5$) upon windbreak porosity. The tabulated values give the downwind distance in multiples of fence height at which recovery to 60% (in brackets 80%) of the approach windspeed occurs

| Source | Hagen et al. [2] atmosphere | Raine and Stevenson [24] wind tunnel | Hagen and Skidmore [25] atmosphere | Numerical (LRR20C) |
|---|---|---|---|---|
| $H/z_0$ | 75 | 100 | 260 | 600 |
| *Porosity* | | | | |
| $k_r = 1$ | | | | (21) |
| 60% | 7.5 | | 12(20) | |
| 50% ($k_r$=2) | | 7.5(16) | | (26) |
| $k_r = 3$ | | | | (28) |
| 40% | 9 | | 13(22) | |
| 34% | | 10(17.5) | | |
| 20% | 12 | 13(22) | 14(19) | |
| 0% | | 13(20) | 14.5(20) | |

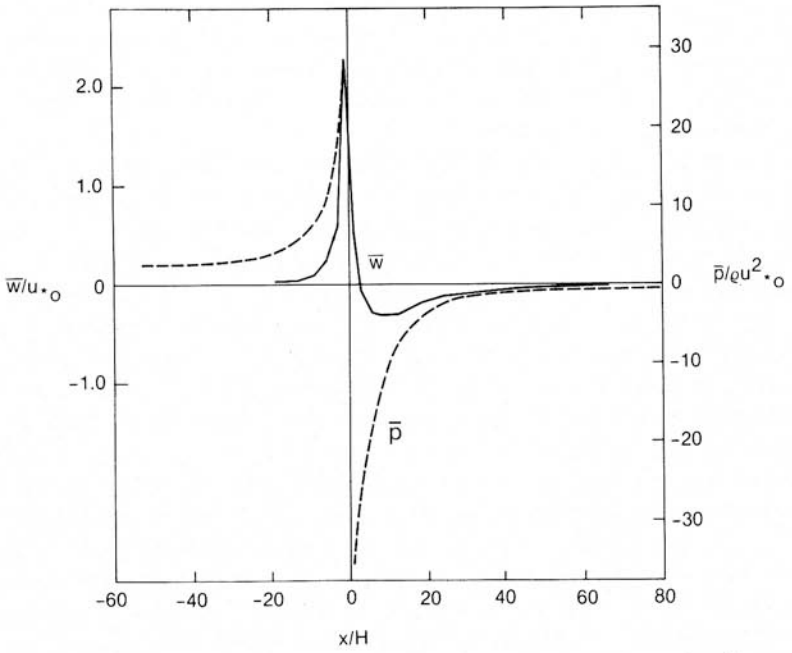


Fig. 11. Horizontal profile of vertical velocity at $z/H = 1.3$ (——) and ground level pressure (— · · —) according to LRR20C scheme.

was that of flow at normal incidence to the fence. It was felt that an attempt to include sensitivity of $k_r$ to angle of attack was unwarranted, because actual inclination angles are fairly small, and in any case large changes in $k_r$ do not yield an improvement in the prediction of the speed-up zone.

Also shown in Fig. 11 is the horizontal profile of ground-level mean pressure, $\bar{p}$, predicted by LRR20C. The ground-level pressure at $x/H = 112$ was given the reference value 0.0 (as discussed by Patankar [17] in the present case only differences in pressure are meaningful and pressure is a relative variable). It is initially surprising to see a pressure difference between $x/H = -60$ and $x/H = +112$ (small though it is relative to the pressure difference across the fence). However, Good and Joubert [27] observed an abrupt pressure rise at a distance $x/H = 15(\delta/H)^{0.7}$ upstream of a solid fence in a smooth-wall wind-tunnel boundary layer (for $0.5 \leqslant \delta/H \leqslant 25$). Though their flow is not strictly comparable, if one applies their finding using boundary layer depth $\delta$ = top level of grid, a pressure rise at $x/H = -220$ is indicated. Therefore, the modest pressure difference predicted between $x/H = -60$ and $x/H = +112$ is not impossible. The predicted difference yields a large term in the volume-integrated force budget (see Section V. C).

As anticipated by Plate [1], the predicted pressure on the back of the fence is constant (to within 1% for $x/H = 1$, $z/H \leqslant 1$) while on the front surface there is greater variation (25% range at $x/H = -1$).

Failure to predict the speed-up over the fence has been shown to be a feature which is independent of the closure scheme employed, and similar defects have been noted in earlier (independent) work*. A possible explanation is that none of the closure schemes deal correctly with mean streamline curvature, which may have very large effects on shear flow turbulence. Bradshaw [28] argued that empirical modification of the Reynolds stress and length scale (dissipation) transport equation is necessary to account for curvature effects, which are much larger than would be expected on the basis of the magnitude of the extra terms arising when the equations are re-cast in a coordinate system appropriate to flow curvature. The convex-upwards streamline curvature over the top of the windbreak implies a stabilising (exchange-suppressing) influence which perhaps brings about the shallow distinct speed-up zone observed. The smallest value of the radius of curvature predicted is approximately $R = 15H$ (at $x=0, z/H = 1$). Though there is no obvious choice for shear layer depth $\delta$, using $\delta \approx 10H$ gives $\delta/R \approx 0.7$, at which value strong curvature effects may be expected [29]. Finnigan and Bradley analysed the TKE budget of this flow and found that the explicit curvature terms were of relatively minor importance. However, as stated above, the possibility (or likelihood) remains that streamline curvature has a large indirect effect on this flow. Incorporation of the curvature correction to the "$k$—$\epsilon$" model suggested by Launder et al. [30], a modification of the $\epsilon$-destruction term based on a local curvature Richardson number, yielded changes in the numerical solution which did not substantially improve the prediction of the flow over the fence. Hanjalic and Launder [31] described a modification of the $\epsilon$-equation which they found improved simulation of a boundary layer with adverse pressure gradient. When included, this modification, which augments the effect of normal strain relative to shear strain on the $\epsilon$-production term, did not significantly alter the prediction of the LRR20C scheme.

Any of the models examined herein will give a satisfactory estimate of the near-ground maximum velocity deficit (i.e., the peak shelter effect) for an isolated belt. However, the failure to give the correct rate of recovery indicates that simulation of multiple windbreaks should be undertaken with special caution. The reason for the good agreement near the windbreak is probably that in this region the pressure gradients are so strong as to dominate the momentum equations, making the stress-gradient parameterisation of secondary importance. Further downstream the pressure gradients are of secondary importance, and stress gradients restore the flow towards equilibrium.

---

*Inadequate grid resolution cannot be ruled out as a possible factor in the failure to predict the flow pattern correctly. No consistent trend with improving resolution has been obtained.

*B. Reynolds stress, turbulent kinetic energy*

It has been shown that, regardless of closure scheme, the numerical models predict a weak speed-up zone over a large depth above the fence rather than the distinct and shallow peak observed. Figure 12 shows that in the speed-up zone of the observations the predicted stress gradients $-\partial u'w'/\partial z$ are strongly negative ($\bar{u}$-momentum sink) whereas the observed values are very small. Figure 13 shows the horizontal profile of ground-level local friction velocity $u_*/u_{*0}$. The predicted values are very sensitive to the choice of lower boundary condition on momentum flux (the $K$—$\bar{e}$—$\epsilon$ prediction shown used $u_*(\bar{u}, \bar{e})$, and the prediction using $u_*(\bar{u})$ differs considerably). The LRR20C prediction is in best overall agreement with the observations.

For some applications the effect of a windbreak on the turbulence is as important as the effect on the mean flow. A reasonably consistent picture of the effect of a fence on the turbulent kinetic energy level in its wake may be drawn from the several wind-tunnel and atmospheric studies available (which span a wide range of values of $H/z_0$ and porosity; in some cases inadequate anemometer frequency response has probably lead to underestimates of high-frequency variance). Where quoted below the results of Raine and Stevenson [24] (RS) for the $u'^2$ variance spectrum have been re-calculated as $nS(n)$ versus ln $nz/\bar{u}$ (an area-preserving scaling which is known

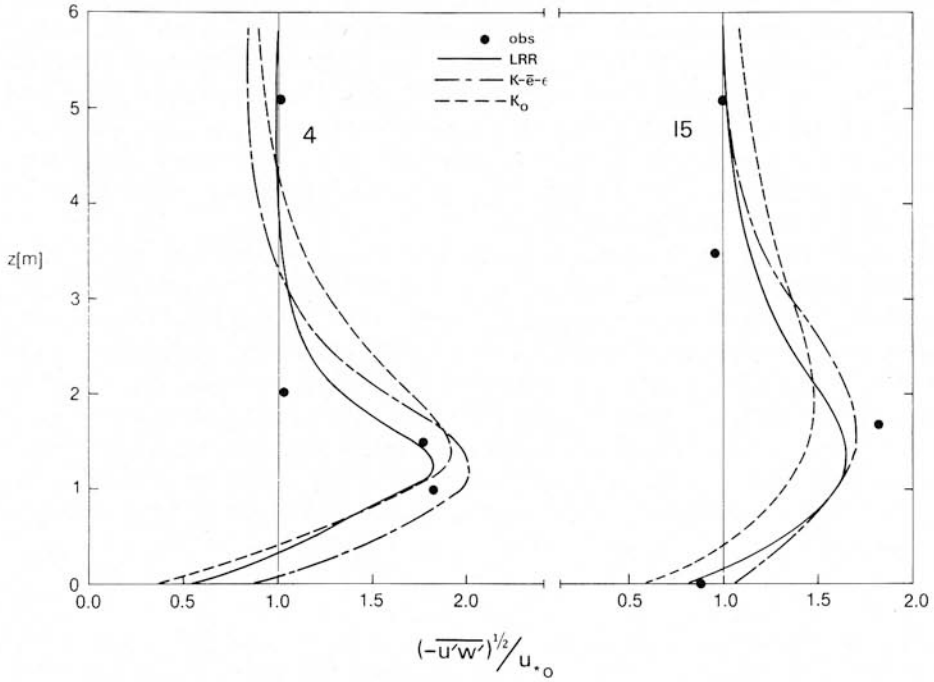


Fig. 12. Vertical profiles of $\sqrt{-\overline{u'w'}}/u_{*0}$ at $x/H$ = (4.2, 15) according to the $K_0$, $K$—$\bar{e}$—$\epsilon$ and LRR20C schemes. Observations (•).

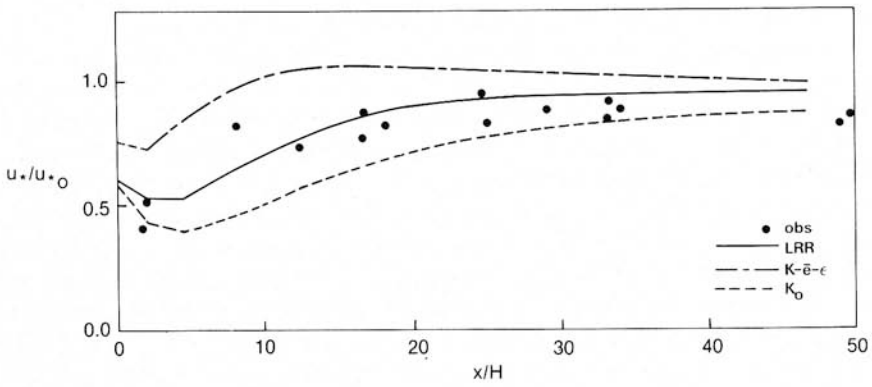


Fig. 13. Horizontal profile of local friction velocity $u_*/u_{*0}$ according to LRR20C, $K$—$\bar{e}$—$\epsilon$ and $K_0$. Observations (•).

to "collapse" equilibrium surface boundary-layer spectra to a universal form) to allow comparison of their measurements from different heights (here $n$ is true frequency). The major features of the TKE field in flow about a fence are:

*(i) Quiet zone*

A zone of reduced $\overline{u'^2}$ and $\overline{v'^2}$ variance in the immediate wake of both solid and porous fences, bounded approximately by a line drawn from the top of the fence to the ground at $x \approx 8H$ (Raine and Stevenson [24]; Hagen and Skidmore [25] (HS)). The extent of the reduction in variance is dependent on porosity; HS reported a 50% reduction in $\overline{u'^2}$ behind a solid fence, a 90% reduction behind porous fences. The RS spectrum at $x/H = 2$, $z/H = 0.6$ for a 50% porous fence shows a dramatic reduction in power in the (normally energy-containing) low-frequency region with a surplus at high frequency, the total variance being only 25% of the upstream value. The peak frequency at this location is strongly dependent on porosity, increasing approximately 10-fold as porosity increases from 0 to 60% which suggests a trend from dominating large eddies to a field of small scale eddies shed by individual elements of the fence. The RS spectra at $x/H = 6$, $z/H = 0.6$ are towards or at the outer edge of the zone of reduced turbulence. The measured variance differed little from the approach value, and the peak frequency showed no sensitivity to porosity. However, there was a distinct change in the spectral distribution of the energy relative to the approach spectrum, the peak frequency being moved to higher frequency (from $n_p \approx 5$ Hz at equilibrium to $n_p \approx 17$ Hz; note that $0.1u_0(H)/H \approx 23$ Hz) with reduced power at very low frequency and increased power elsewhere.

*(ii) Turbulent zone*

A large increase in TKE centred on the streamline touching the top of a porous fence (in the case of a solid fence, along a streamline passing through

$z \approx 1.5H$ at the fence; RS) with a maximum value at about $x/H = 10$ and farther downstream progressive diffusion and weakening (Finnigan and Bradley). According to Finnigan and Bradley, above this fence-top streamline TKE is increased by at least 50% at all levels observed ($z/H \leqslant 4$) in the range $4 \leqslant x/H < 40$ = farthest downstream observation. Raine and Stevenson and HSMK indicate that increases do not occur above about $z/H = 3$.

Ogawa and Diosey [32] present simultaneous spectra at $z = H$ upwind and downwind of a solid fence in the atmospheric surface layer. Their use of normalised frequency $nH/\bar{u}_0(H)$ (where $\bar{u}_0(H)$ = upstream windspeed at $H$ and $n$ = true frequency) means that one may readily compare the spectral variance as a function of true frequency. The observation at $x/H = 5$, $z/H = 1$ falls in the zone of increased variance. The peak frequency of the $\overline{u'^2}$, $\overline{v'^2}$ spectra is displaced upwards in frequency (relative to the approach spectra). Though the variance at very low frequency is reduced, the total variance is increased by $\sim$ 50%. The peak of the $\overline{w'^2}$ spectrum at this location is displaced downwards in frequency (but by $x/H = 10$ has returned to the equilibrium position). Ogawa and Diosey interpret these contrasting results for horizontal and vertical velocity spectra by hypothesising that the airflow/solid-fence interaction generates eddies at frequencies which are high relative to dominant frequencies in the equilibrium horizontal velocity spectra but low relative to the dominant frequencies in the equilibrium vertical velocity spectrum. At $x/H = 5$ the spectra of all three velocity components peak at $n_p H/\bar{u}_0(H) \approx 0.1$ which suggests that $n_p = 0.1\bar{u}_0(H)/H$ is a figure representative of the frequency at which the interaction between a solid fence and the airflow contributes turbulent energy. This estimate predicts $n_p = 23$ Hz (precisely as observed) for the RS wind-tunnel observation of the $\overline{u'^2}$ spectrum at $x/H = 6$, $z/H = 0.6$ behind a solid barrier, and is a reasonable first estimate (in the absence of a better method) for the peak frequency outside the zone of reduced turbulence behind porous fences.

According to Raine and Stevenson, by $x/H = 15$ spectra of $u'^2$ have regained the shape of approach spectra but with the peak frequency remaining higher than that at equilibrium and with increased total variance.

The zone of increased TKE may be explained by an increased shear production rate. The air flow—fence interaction converts both mean kinetic energy and low frequency turbulent kinetic energy to high frequency wake turbulence. The existence of a quiet zone may be qualitatively understood if one accepts the hypothesis that the wake turbulence, having a very small length scale, is rapidly dissipated. Certainly wake turbulence is not a major part of the total TKE within a plant canopy, where (as is the case at a windbreak) the MKE $\rightarrow$ TKE conversion rate can be large with respect to the local (shear) production rate (see ref. 9). If one starts with the inclusion (which seems very reasonable) of a body force in the instantaneous $u$-momentum equation which removes momentum in proportion to the instantaneous velocity

$$\frac{\partial u}{\partial t} + \frac{\partial}{\partial x}\,(u^2 + p/\rho) + \frac{\partial}{\partial z}\,(uw) = -k_r u|u|\delta(x, 0)\, s(z,H) \tag{21}$$

it follows that in the derived Reynolds averaged equations these are extra terms in $k_r$ as follows

$$\frac{\partial \bar{u}}{\partial t} + \ldots = \ldots - k_r(\bar{u}^2 + \overline{u'^2})\,\delta(x, 0)\, s(z,H) \tag{22a}$$

$$\frac{\partial \overline{u'^2}}{\partial t} + \ldots = \ldots - 4k_r\bar{u}\,\overline{u'^2}\,\delta(x, 0)\, s(z,H) - 2k_r\overline{u'^3}\,\delta(x, 0)\, s(z,H) \tag{22b}$$

$$\frac{\partial \overline{u'w'}}{\partial t} + \ldots = \ldots - 2k_r\,\bar{u}\,\overline{u'w'}\,\delta(x, 0)\, s(z,H) - k_r\overline{u'u'w'}\,\delta(x, 0)\, s(z,H) \tag{22c}$$

Thus, a sink for $\overline{u'^2}$ arises naturally (treatment of the $\overline{v'^2}$ and $\overline{w'^2}$ equations is more difficult since these fluctuations are parallel to the fence rather than normal), and provided it is understood that this energy must reappear (with the extracted MKE) at high frequency, this seems a reasonable explanation and approach to take in modelling. Since the numerical models cannot represent changes in spectral distribution, and the dissipation rate equation, $\epsilon$, is matched to the equilibrium spectral distribution, the reappearance of the "missing energy" must be neglected (else it causes an erroneous rise in total TKE in the near wake as noted earlier).

Turning now to the numerical simulations, Fig. 14 shows the prediction of LRR20C for the streamwise profile of $\overline{u'^2}/(\overline{u'^2})_0$ at fixed heights $z/H$ = 0.25, 0.5, 1.0, 4.0 (for the Bradley and Mulhearn fence). The extra sink terms in $k_r\bar{u}$ which appear in eqns. (22b) and (22c) were included; without them, the zone of reduced turbulence is not predicted (though ground-level values of TKE are reduced because they are determined via $u_*$ from the near-ground horizontal velocity). The mean velocity field is only slightly modified as a result of including these terms and is in no less satisfactory agreement with observation. The triangular zone of reduced variance in the immediate lee of the fence is in qualitative agreement with the findings of Raine and Stevenson as to the degree of reduction and rate of recovery for a fence of 50% porosity. A corresponding plot of TKE yields a very similar pattern, the main difference being that the minima occur at $x/H$ = 2 rather than at the fence, and are not as deep ($\bar{e}/\bar{e}_0 \approx 0.4$ at $z/H$ = 0.25, 0.5). At $z/H$ = 1.0 the predicted TKE rises sharply behind the fence and reaches a peak of $\sim 2.5\bar{e}_0$ at $x/H \approx 10$. This may be compared with the variation of TKE along Finnigan and Bradley streamline 2, which far upstream lies at $z/H \approx 0.7$. The observations indicate a peak at $x/H \approx 10$ of about the same magnitude as that predicted. At $z/H$ = 4.0 the TKE remains at the far upstream level $\bar{e}_0$ except downstream of $x/H \approx 10$ where a very modest rise is evident. This is in contrast to the observations of FB, who found that above their streamline 2 the TKE is enhanced by at least 50% at all ob-

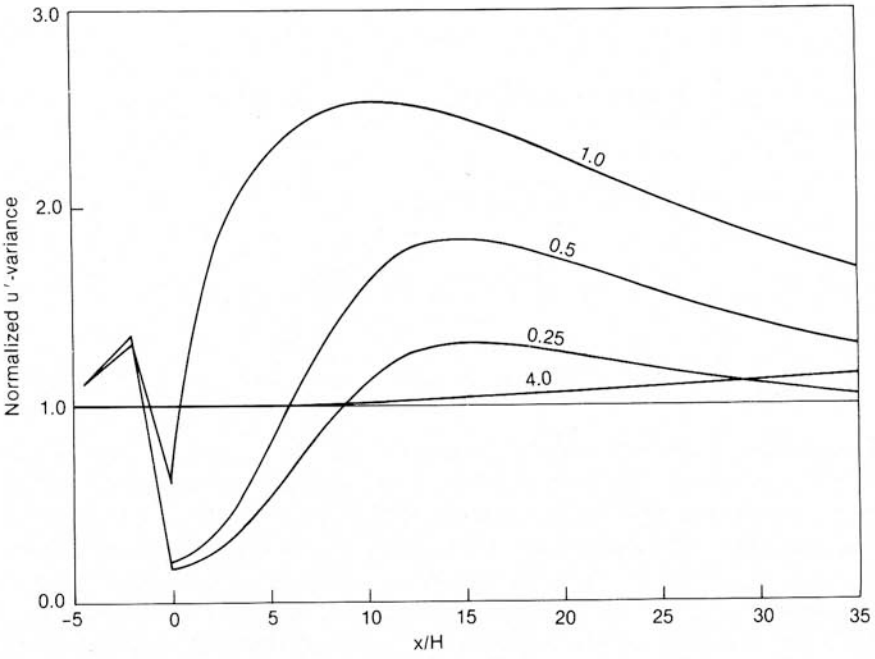


Fig. 14. Horizontal profiles of $\overline{u'^2}/(\overline{u'^2})_0$ at $z/H$ = 0.25, 0.5, 1.0, 4.0 according to the LRR20C scheme.

served points. This (enhanced) level of the TKE was observed to remain rather constant with downstream position, at least over the range $4.2 < x/H < 40$. FB suggest that this enhancement of the TKE at large $z$ is caused by turbulent and pressure transport; these have been modelled using a gradient-diffusion term. The poor agreement as to the TKE level between model and observation at large $z$ may indicate that this closure assumption is a major weakness. On the other hand, enhancement of the TKE at large $z$ has not been reported in other studies.

*C. The integral force balance*

The integral force balance was always performed over the volume defined by the computational boundaries. The results of the force balance varied with the closure scheme employed and the size of the domain (the latter being expected, of course). One unambiguous indication is that even with a very large domain, $D_s = [-60{:}112, 47]^{24}_{10,13}$, the term $[\bar{u}^2 + \overline{u'^2} + \frac{\bar{p}}{\rho}]^{x2}_{x1}$ may not be neglected. Table 3 gives the force balance according to the $K_0$, $K$—$\bar{e}$—$\epsilon$, and LRR20C schemes. Whether or not the overwhelming importance of the pressure term is real or an artificiality of the numerical models is uncertain. Seginer [33] applied Bernoulli's Theorem to the velocity pattern about a windbreak and deduced that with $X1 \approx 10H$ and $X2 \approx 30H$ the pressure

TABLE 3

Integral force balance according to $K_0$, $K$—$\bar{e}$—$\epsilon$, and LRR20C schemes for standard domain $D_s$

| | $K_0$ | $K$—$\bar{e}$—$\epsilon$ | LRR20C |
|---|---|---|---|
| $[\bar{u}^2]_{X1}^{X2}/FD^a$ | −0.45 | −0.81 | −0.58 |
| $[\overline{u'^2}]_{X1}^{X2}/FD^a$ | 0.00 | −0.08 | −0.03 |
| $[\bar{p}/\rho\ u_{*0}^2]_{X1}^{X2}/FD^b$ | +1.16 | +1.87 | +1.43 |
| $[\overline{u'w'}]_{z_0}^{ZT}/FD^c$ | +0.31 | +0.03 | +0.19 |

[a] Positive if influx exceeds outflux.
[b] Positive if inflow pressure exceeds outflow pressure.
[c] Positive if momentum flux to ground is smaller than momentum flux to top boundary.

term makes only a small contribution to the overall budget. However, the use of Bernoulli's Theorem in this context is rather crude.

## VI. Design of an isolated windbreak

The numerical models, particularly LRR20C, have given an accurate prediction of the decrease in windspeed in the near wake of a windbreak (see Fig. 10). The LRR20C model has therefore been used to investigate the velocity deficit and the drag over a range of values of the parameters $H/z_0$ and $k_r$ with the aim of providing design guidelines.

Figure 15 gives the horizontal profile of $\bar{u}(z)/\bar{u}_0(z)$ at $z/H = 0.6$ for several values of $H/z_0$ and $k_r = 0.5, 5.0$. The shift in the location of the speed minimum towards the windbreak as the porosity is decreased agrees with wind-tunnel and atmospheric observations. Though reservations have been expressed as to the accuracy of the far wake, there is no reason to doubt the accuracy of the predicted near-wake velocity minimum*, the depth of which can be seen to be rather insensitive to large changes in $H/z_0$. These (and other) numerical predictions may be conveniently summarised by defining a fractional velocity reduction (or index of shelter effectiveness)

$$I_{SE} = \frac{\bar{u}_0(z) - \bar{u}(x, z)}{\bar{u}_0(z)} = \frac{\Delta\bar{u}(z)}{\bar{u}_0(z)}$$

The variation of $I_{SE}$ with changing $H/z_0$ and $k_r$ is shown in Fig. 16; ($I_{SE}$ has been evaluated at the downstream distance of greatest speed reduction at height $z/H = 0.6$). This variation may be described by the formula

*Though the solutions obtained are not grid-independent, the changes in the near-ground velocity field immediately behind the fence brought about by changing the grid resolution are not a large fraction of the observed velocity reduction ($\lesssim 5\%$).

$$\frac{\Delta \bar{u}}{\bar{u}_0} = 0.19 \ln(k_r) + 0.42$$

Given $k_r$, the maximum velocity reduction (i.e., the depth of the wind reduction curve) may be deduced with an expectation of errors not exceeding

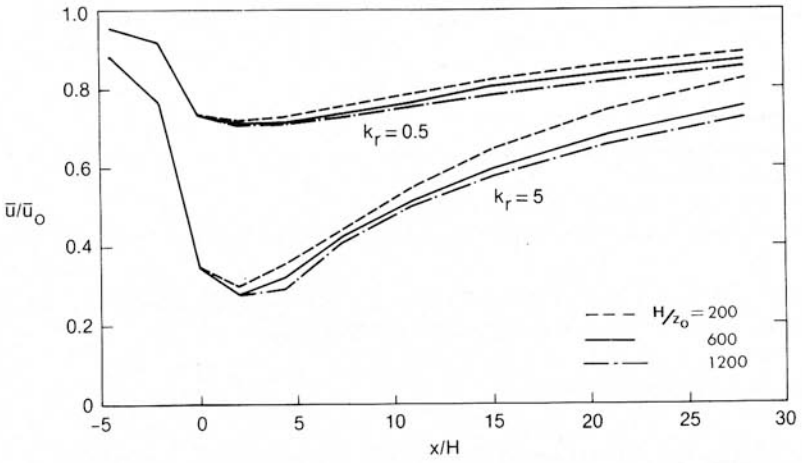


Fig. 15. Horizontal profile of relative windspeed $\bar{u}(z)/\bar{u}_0(z)$ at $z/H = 0.6$ according to LRR20C for several values of $H/z_0$ and $k_r = 0.5, 5.0$.

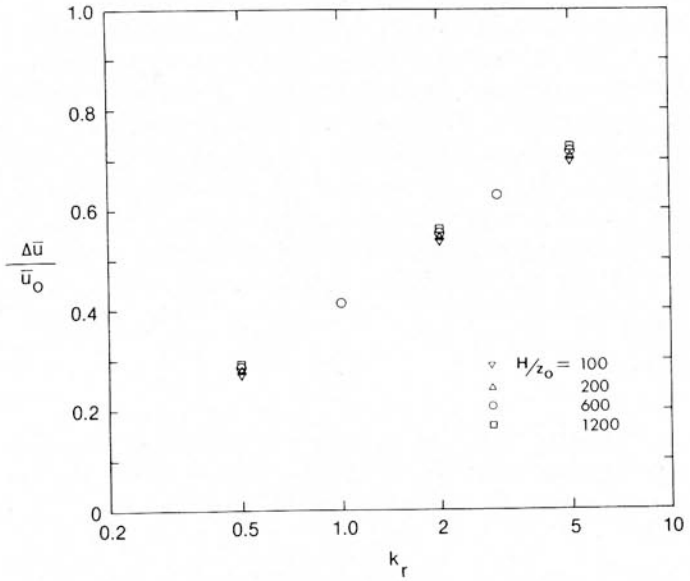


Fig. 16. Fractional reduction in windspeed $\Delta \bar{u}(x, z)/\bar{u}_0(z)$, where $\bar{u}_0$ is the approach speed, evaluated at ($x/H$ = location of minimum; $z/H = 0.6$) as a function of $H/z_0$ and $k_r$.

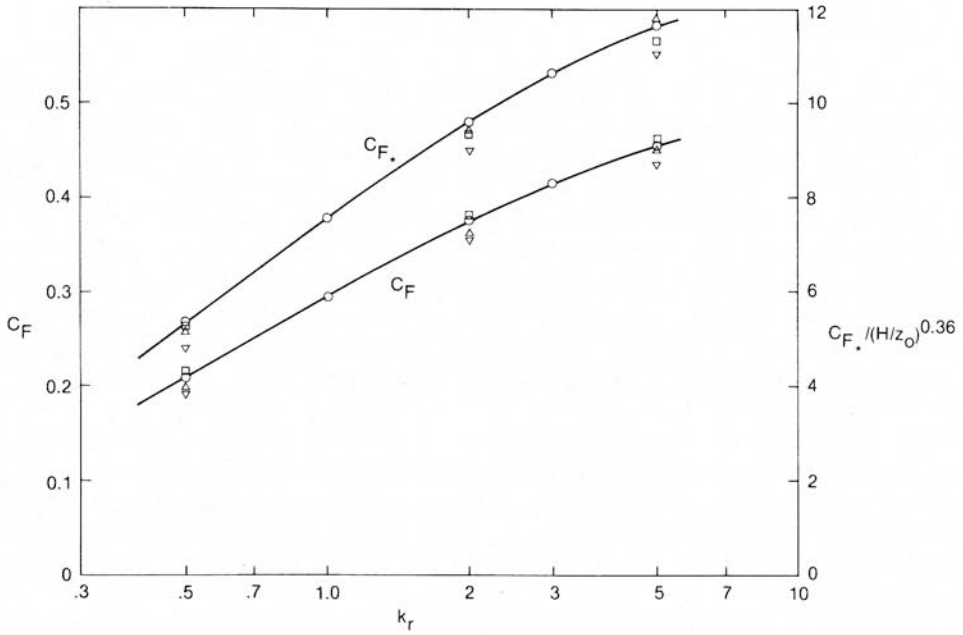


Fig. 17. Variation of the drag (per unit crosswind length) on a fence with $H/z_0$, $k_r$. Symbols denote values of $H/z_0$ as defined on Fig. 16.

20%*. Values of $k_r$ may be related to screen/fence type and porosity with the aid of engineering correlations, such as those given by Hoerner [19]. For natural windbreaks, the value of $k_r$ may be roughly estimated as

$$k_r \approx \int_{-\infty}^{+\infty} c_D a_{LB} \, dx$$

where $a_{LB}$ is the leaf (or branch) area density and $c_D$ is a corresponding drag coefficient.

It is useful to define

$$C_{F*} = \frac{D}{\rho u_{*0}^2 H} \qquad C_F = \frac{D}{\rho \, \bar{u}_0^2(H) H}$$

where $D$ is the drag on the fence per unit crosswind length. It is not possible to deduce the fence drag coefficients from a knowledge of $k_r$ because their values depend on the wind profile at the fence, hence, on the flow pattern in its entirety. However, the predictions of the numerical model may be used to determine $C_F$, $C_{F*}$ as a function of $k_r$, $H/z_0$. Figure 17 shows the variation of $C_F$ and $C_{F*}/(H/z_0)^{0.36}$ against $k_r$ according to LRR20C; from these curves the drag per unit length on a fence may be determined simply by specifying $k_r$ and either $(H/z_0, u_{*0})$ or $(H, \bar{u}_0(H))$.

*The range of validity of these predictions is uncertain, and it is inadvisable to extrapolate very far in the direction of low porosity (high $k_r$).

## VII. Conclusions

Of the closure schemes examined here, the Reynolds-stress model first proposed by Launder et al. [15] has proven most accurate, and has given very satisfactory agreement with observations of the velocity in the near wake of a fence with minimal input (specification of the pressure loss coefficient, $k_r$, as determined by a simple wind-tunnel test). The gain in accuracy obtained by using second-order closure rather than simpler alternatives is modest, and surprisingly good predictions of the near wake are obtained using the very crude assumption of an eddy viscosity varying with height alone, $K_0(z) = 0.4u_{*0}z$. This is probably a consequence of dominance of pressure gradients and relative unimportance of stress gradients near the windbreak.

Provided that one includes a sink term in the $\overline{u'^2}$ budget equation to convert low-frequency power to wake turbulence (which is assumed to be dissipated rapidly), the Reynolds-stress model also gives a satisfactory prediction of the triangular zone of reduced TKE in the immediate lee of a fence, and of the zone of increased TKE centred on the streamline touching the top of the fence.

A general feature of these simulations (which has also been noted in independent work) is a failure to predict the sharp speed-up zone observed above the fence and a consequently underestimated rate of return towards the upstream equilibrium state. This is believed to indicate inadequacy of the closure schemes in this very complex flow which contains strong streamline curvature. Though there are other aspects of the numerical models which are not above criticism (e.g., the lower boundary condition on the stresses; the simple momentum sink), large alterations in these areas have not yielded significant change*.

Because of the good agreement between observation and prediction in the near wake, it has been possible to give design aids relating the expected speed reduction near an isolated fence and the drag on the fence to the key fence parameter $k_r$. However, the unsatisfactory prediction of the far wake means that one could not with confidence simulate the more complex problem of a windbreak network.

## Acknowledgements

This work was started while the author was at the New Zealand Meteorological Service and has been completed at the University of Guelph under the partial support of the National Science and Engineering Research Council of Canada. I am grateful to Dr. E.F. Bradley for sending me his experimental data, and to Dr. G.D. Stubley for easing my introduction to the

*As noted earlier, inadequate grid resolution may have contributed to the deficiencies of the solutions given.

SIMPLE numerical method. I would also like to thank the many people with whom I have had encouraging discussions, in particular Dr. R.A. Wooding and Dr. R.H. Shaw.

## References


1 E.J. Plate, The aerodynamics of shelter belts, Agric. Meteorol., 8 (1971) 203–222.
2 L.J. Hagen, E.L. Skidmore, P.L. Miller and J.E. Kipp, Simulation of effect of wind barriers on airflow, Trans. ASAE, 24 (1981) 1002–1008.
3 F. Durst and A.K. Rastogi, Turbulent flow over two-dimensional fences, in Turbulent Shear Flows, Vol. 2, Selected papers from the 2nd Int. Symp. on Turbulent Shear Flows, London, 1979, Springer-Verlag, Berlin, 1980, pp. 218–232.
4 J. Counihan, J.C.R. Hunt and P.S. Jackson, Wakes behind two-dimensional surface obstacles in turbulent boundary layers, J. Fluid Mech., 64 (1974) 529–563.
5 M.D.A.E.S. Perera, Shelter behind two-dimensional solid and porous fences, J. Wind Eng. Ind. Aerodyn., 8 (1981) 93–104.
6 J.J. Finnigan and E.F. Bradley, The turbulent kinetic energy budget behind a porous barrier: an analysis in streamline coordinates, J. Wind Eng. Ind. Aerodyn., 15 (1983) 157–168.
7 E.F. Bradley and P.J. Mulhearn, Development of velocity and shear stress distributions in the wake of a porous shelter fence, J. Wind Eng. Ind. Aerodyn., 15 (1983) 145–156.
8 N.R. Wilson and R.H. Shaw, A higher order closure model for canopy flow, J. Appl. Meteorol., 16 (1977) 1197–1205.
9 M.R. Raupach and R.H. Shaw, Averaging procedures for flow within vegetation canopies, Boundary-Layer Meteorol., 22 (1982) 79–90.
10 E.M. Laws and J.L. Livesey, Flow through screens, Ann. Rev. Fluid Mech., 10 (1978) 247–266.
11 J.D. Wilson, D.P. Ward, G.W. Thurtell and G.E. Kidd, Statistics of atmospheric turbulence within and above a corn canopy, Boundary-Layer Meteorol., 24 (1982) 495–519.
12 J.C.R. Hunt, D.P. Lalas and D.N. Asimakopoulos, Air flow and dispersion in rough terrain: a report on Euromech 173, J. Fluid Mech., 142 (1984) 201–216.
13 B.E. Launder and D.B. Spalding, The numerical computation of turbulent flows, Comput. Methods Appl. Mech. Eng., 3 (1974) 269–289.
14 G. Mellor, Analytic prediction of the properties of stratified planetary surface layers, J. Atmos. Sci., 30 (1973) 1061–1069.
15 B.E. Launder, G.J. Reece and W. Rodi, Progress in the development of a Reynolds-stress turbulence closure, J. Fluid Mech., 68 (1975) 537–566.
16 S.B. Pope and J.H. Whitelaw, The calculation of near-wake flows, J. Fluid Mech., 73 (1976) 9–32.
17 S.V. Patankar, Numerical Heat Transfer and Fluid Flow, Series in Computational Methods in Mechanics and Thermal Sciences, Hemisphere Publishing Co., London, 1980.
18 J.P. Van Doormaal and G.D. Raithby, Enhancements of the SIMPLE method for predicting incompressible fluid flows, Numerical Heat Transfer, 7 (1984) 147.
19 S.F. Hoerner, Fluid Dynamic Drag, S.F. Hoerner, Library of Congress Catalog Card Number 64-19666, 1965.
20 W.D. Baines and E.G. Peterson, An investigation of flow through screens, Trans. ASME, 73 (1951) 467–480.
21 M.M. Gibson and B.E. Launder, Ground effects on pressure fluctuations in the atmospheric boundary layer, J. Fluid Mech., 86 (1978) 491–511.

22 A.K. Rastogi and W. Rodi, Calculation of general three-dimensional turbulent boundary layers, J. AIAA, 16 (1978) 151—159.
23 J. van Eimern, R. Karschon, L.A. Razumova and G.W. Robertson, Windbreaks and Shelterbelts, World Meteorol. Org. Tech. Note No. 59 (1964).
24 J.K. Raine and D.C. Stevenson, Wind protection by model fences in a simulated atmospheric boundary layer, J. Ind. Aerodyn., 2 (1977) 159—180.
25 L.J. Hagen and E.L. Skidmore, Turbulent velocity fluctuations and vertical flow as affected by windbreak porosity, Trans. ASAE, 14 (1971) 634—637.
26 T. Maki and S. Kawashima, Studies on the windbreak nets, J. Agric. Meteorol. (Japan), 39 (1983) 79—89 (in Japanese).
27 M.C. Good and P.C. Joubert, The form drag of two-dimensional bluff plates immersed in turbulent boundary layers, J. Fluid Mech., 31 (1968) 547—582.
28 Bradshaw, P., Effects of streamline curvature on turbulent flow, AGARDograph No. 169 (1973).
29 Bradshaw, P., The analogy between streamline curvature and buoyancy in turbulent shear flow, J. Fluid Mech., 36 (1969) 177—191.
30 Launder, B.E., C.H. Priddin and B.I. Sharma, The calculation of turbulent boundary layers on spinning and curved surfaces, Trans. ASME J. Fluids Eng., 99 (1977) 231—239.
31 K. Hanjalic and B.E. Launder, Sensitizing the dissipation equation to irrotational strains, Trans. ASME J. Fluids Eng., 102 (1980) 34—40.
32 Y. Ogawa and P.G. Diosey, Surface roughness and thermal stratification effects on the flow behind a two-dimensional fence. I. Field study, Atms. Environ., 14 (1980) 1301—1308.
33 I. Seginer, Windbreak drag calculated from the horizontal velocity field, Boundary-Layer Meteorol., 3 (1972) 87—97.